Hunting for primordial galaxies

Tina Ström

Supervisor:
Erik Zackrisson

May 28, 2012

Department of Astronomy - Stockholm University
Thesis for Master of Science in Astronomy
Fall 2011 & Spring 2012

Abstract

Population III galaxies consisting mostly of metal-free stars are predicted to have formed in the early universe, i.e. at high redshift. Here, we derive the color signatures of such exotic objects, using a state of the art spectral synthesis code that can account for e.g. metallicity, age, extinction and initial mass function. The color signatures vary, compared to other published papers that mostly make use of the Lyman break technique to identify high-redshift objects. In our survey, we take into account strong Lyman-α radiation and can therefore detect sources that might be rejected otherwise.

We make use of samples from ultra deep fields in published papers which have identified high-redshift galaxies. Comparing the properties of these objects to our criteria, we discovered a number of strong population III galaxy candidates.

As gravitational lenses boost the flux of objects behind them, we can observe objects that would be too faint for observations in unlensed fields. This provides us with an alternative way of observing the high-redshift universe. We report the discovery of population III galaxy candidates in these fields after applying a set of constraints to ensure a high-redshift sample.

Furthermore, we discuss the strengths and weaknesses of the technique and results.

Contents

1 Introduction

One of the most intriguing questions in modern cosmology is the formation of the first stars. By exploring this subject, it is possible to increase the understanding of how the first stellar systems and supermassive black holes etc. were formed.

The first stars are believed to have been metal-free since no heavier elements have had the time to form at this epoch. As a result of this, a small part of the first galaxies might consist of these stars (Stiavelli & Trenti, 2010). Throughout this thesis we will define a galaxy as a stellar population which can host ongoing star formation for more than one generation of stars.

If the first stars can be observed, we could explore their mass distribution and investigate if they are as massive as our current theory predicts. The first stars are, however, too faint to observe. Our only chance is probably to look for galaxies that host these metal-free stars, but finding these objects is challenging. Not only are they very faint, another difficulty is to distinguish these sources from mundane objects.

We will determine the spectral signatures of the first galaxies, and for this purpose we use the Yggdrasil spectral synthesis model. It can predict the magnitudes of e.g. different stars and stellar populations with different initial conditions such as metallicity, age, initial mass function and extinction. After determining if metal-free galaxies show any distinguishable spectral features and, if so, what they look like, it is possible to start searching for these exotic objects.

The first place to search is in ultra deep fields, which are small areas of the sky that have been exposed for a relatively long time. By increasing the exposure time, more faint objects can be detected. High-redshift samples have been prepared (by e.g. Bouwens et al. (2011) and McLure et al. (2011)) using these observed fields.

Another way of observing objects at very high redshift is to use the telescopes that the universe provides us with; gravitational lenses. By using massive galaxy clusters as gravitational lenses it is possible to explore the high-redshift universe behind them. CLASH (Cluster Lensing and Supernova survey with Hubble) has started to observe a number of galaxy clusters and the data from these has been continuously released during the course of this thesis project.

The aims for this thesis is to use the Yggdrasil code to derive spectral features for metal-free galaxies. Using these results it is possible to start searching for these objects in ultra deep fields and behind galaxy clusters which are being used as gravitational lenses.

In Sect. 2 and 3, I provide the theoretical background for this work. In the next section, I explain Yggdrasil and its features. Sect. 5 contains the case of gravitational lensing and Sect. 6 explores the CLASH survey. In Sect. 7, I give the results of this study and in the final sections I summarize and present the work as well as discussing the outlook for this type of studies.

2 The first stars

The early universe favors more massive stars to form. The mass at which the gas pressure of a cloud no longer can support its weight is called the Jeans mass; it is described by

$$M_{\rm J} \simeq \mu m_{\rm H} n L_{\rm J}^3 \simeq 700 \left(\frac{T}{200{\rm K}}\right)^{3/2} \left(\frac{n}{10^4{\rm cm}^{-3}}\right)^{-1/2} {\rm M}_\odot, \tag{2.1}$$

where $m_{\rm H}$ is the mass of a hydrogen atom, $L_{\rm J}$ is the characteristic size of a "Jeans cloud" and n is the number density of the cloud. The mean molecular weight, μ, is normalized to $\mu = 1.2$, which is the case for neutral primordial gas (Johnson, 2011). As the first gas consisted mainly of hydrogen and helium, the number of coolants was low, leading to a higher temperature.

For higher temperatures, the Jeans mass becomes larger and hence allowing more massive stars to form. Additionally, for higher temperatures the accretion rate (Eq. (2.2)) also increases;

$$\dot{\rm M}_{\rm acc} \simeq \frac{\rm M_J}{t_{\rm ff}} \simeq \left(\frac{T}{200{\rm K}}\right)^{3/2} {\rm M}_\odot\,{\rm yr}^{-1}, \tag{2.2}$$

where $t_{\rm ff}$ is the free-fall time. As the Jeans mass, and thus the accretion rate, increase with higher temperatures, the initial mass function (IMF) in the early universe was probably top-heavy. The first stars are therefore believed to have been very massive with a metallicity close to zero and are called population (pop) III stars.

It is believed that the metal-free stars are formed in dark matter minihalos whose characteristic masses are of the order of $\sim 10^5 - 10^6 M_\odot$ as early as $z \sim 50$ (Yoshida et al., 2003).

The minihalos where the first stars were formed, however, did not likely host the first galaxies. The feedback from the stars in the form of radiation and supernova explosions would disrupt the halo and making future star formation impossible (Bromm & Yoshida, 2011).

As the first stars are believed to have formed in small numbers in minihalos, their integrated brightness is not sufficient to be able to observe them with current telescopes.

3 The first galaxies

As the minihalos are not massive enough to retain their gas after the first stars have formed, it is believed that the first galaxies were formed in halos with higher mass. These higher mass halos are probably mergers of the

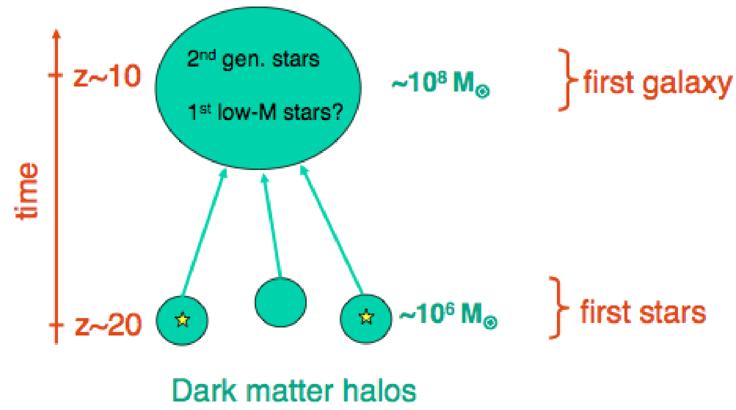

Figure 3.1: Schematic picture of how the first galaxies probably formed. An atomic cooling halo is assembled from several dark matter minihalos. As the first metal-free stars are believed to have formed in these minihalos, second generation stars may be present in the first galaxies. Credit: Bromm & Yoshida (2011).

minihalos as they *re-virialize* the expelled gas (Bromm & Yoshida, 2011). Fig. 3.1 shows the standard scenario for the formation of the first galaxies.

If the dark matter halo is more massive than $\sim 10^7 - 10^8 M_\odot$, gravity could withstand the forces from the first supernovae and retain the gas inside the halo after a star formation period, (Johnson, 2011; Bromm & Yoshida, 2011). This would give rise to the first galaxies at $z \leq 15$ (e.g. Johnson et al., 2008).

The virial temperature for a dark matter halo massive enough to withstand the forces of the feedback from the stars is described by

$$T_{\rm vir} \simeq 4 \times 10^4 \left(\frac{\mu}{1.2}\right) \left(\frac{M_{\rm h}}{10^8 h^{-1} {\rm M}_\odot}\right)^{2/3} \left(\frac{1+z}{10}\right) {\rm K}, \tag{3.1}$$

where $M_{\rm h}$ is the halo mass, z is the redshift, μ is the mean molecular weight of the gas, $h = H_0/100$, and H_0 is the Hubble constant given in km s^{-1} Mpc^{-1} (Johnson, 2011). Eq. (3.1) is normalized to $\mu = 1.2$, which is the case for a primordial neutral gas (Johnson, 2011). Assuming a cold dark matter cosmological model with a cosmological constant (ΛCDM) and $h \simeq 0.7$, at $z \sim 20$ and $\rm M_h \sim 10^7$ $M_\odot$, the virial temperature is roughly $T_{\rm vir} \approx 10^4$ K. At this temperature, the gas starts to ionize; a significant fraction of the energy released from a supernova in this environment is transformed to emission and is radiated away. This significantly reduces the gas that is ejected from the halo, compared to if there was no photoionization (Johnson, 2011).

Another characteristic property of a dark matter halo is its virial radius, which is the distance from the center where the infalling material reaches

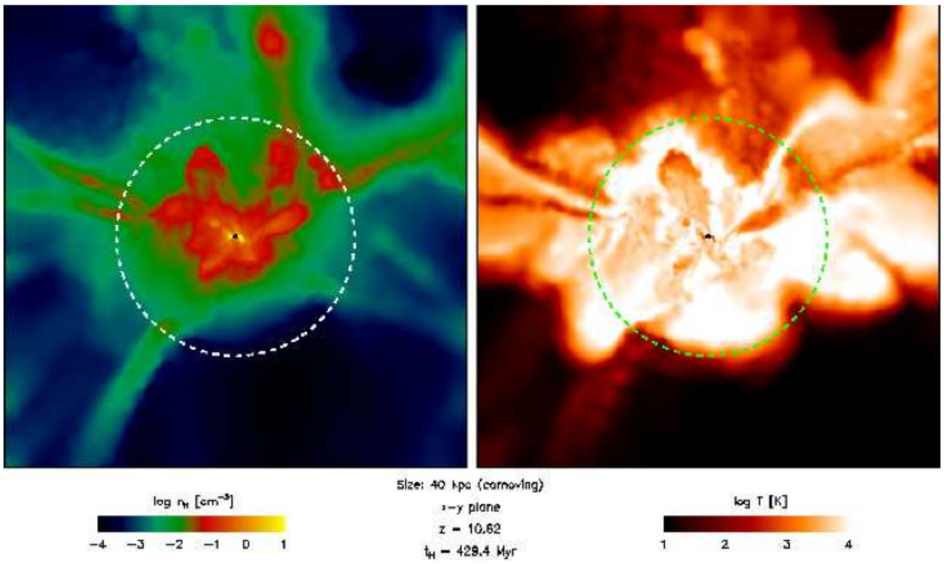

Figure 3.2: Gas collapsing into a dark matter halo at $z \approx 10$. The left panel corresponds to the number density of hydrogen and the right panel is the temperature. The dashed line shows the virial radius. Credit: Greif et al. (2008b).

the virial temperature (Johnson, 2011). Fig. 3.2 shows a simulation of a dark matter halo massive enough to host the first galaxy. The infalling matter from the intergalactic medium (IGM) reaches the virial temperature at $r_{\mathrm{vir}} \approx 1$ kpc.

Some of the gas, however, does not reach the virial temperature. Instead it continues to stream to the center where it can cool the existing gas to < 500 K, and later collapse to form stars (Johnson, 2011).

At temperatures above 10^4 K, part of the gas is ionized. The dominant reaction in creating hydrogen molecules is

$$\mathrm{e}^- + \mathrm{H} \rightarrow \mathrm{H}^- + \gamma \tag{3.2}$$

$$\mathrm{H}^- + \mathrm{H} \rightarrow \mathrm{H}_2 + \mathrm{e}^-. \tag{3.3}$$

As the gas is partly ionized, the electron fraction is enhanced, and the reaction rate of Eq. (3.2) increases and the density of molecular hydrogen becomes larger at the center of the halo. Additionally, a higher density of H_2 triggers another reaction where a deuterium nucleus reacts with a hydrogen molecule to form deuterium hydride and a hydrogen atom:

$$\mathrm{D}^+ + \mathrm{H}_2 \rightarrow \mathrm{HD} + \mathrm{H}^+. \tag{3.4}$$

As the primordial gas contains a very low free electron fraction, $X_\mathrm{e} \leq 10^{-4}$ (Johnson, 2011), Eqs. (3.2) and hence (3.3) and (3.4) are inefficient. The enhanced density of H_2 in the halos that hosted the first galaxies thus

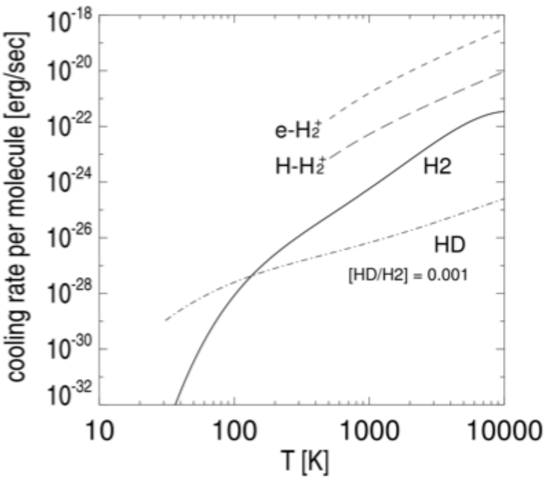

Figure 3.3: The cooling rates for H_2(solid line), HD(dot-dashed line) and H_2^+(dashed lines). Credit: Johnson (2011).

leads to a more efficient cooling than in the minihalos that created the first pop III stars.

As can be seen from Fig. 3.3, at low temperatures the HD-cooling is more efficient than for H_2; this leads to even lower temperatures in the center of the halo. It is not shown in Fig. 3.3, but at T $\sim 10^4$ K, the most efficient coolant is atomic hydrogen (Johnson, 2011). The halos that formed the first galaxies are therefore usually referred to as *atomic cooling halos*.

However, the situation becomes more complicated after the first stars have formed. They emit, for instance Lyman-Werner photons; these are photons with energies ranging from 11.2 to 13.6 eV (Johnson, 2011). These high energy photons can dissociate the hydrogen molecules according to

$$\mathrm{H_2} + \gamma \rightarrow \mathrm{H_2^*} \rightarrow 2\mathrm{H}. \tag{3.5}$$

As a consequence, the cooling by H_2 is suppressed and the star forming phase is delayed (Johnson, 2011).

Additionally, the first pop III stars may affect other zero-metallicity stars formed at later times. The radiation emitted from the stars can dissociate neutral hydrogen:

$$\mathrm{H} + \gamma \rightarrow \mathrm{H^+} + \mathrm{e^-}. \tag{3.6}$$

The free electron can collide with other gas particles and thus heating the gas. The temperature at which these reactions are are at equilibrium is $T \sim 10^4$ K. However, when stars within the halo die, the temperature decreases. This enables HD molecules to form and the temperature can reach as low values as $T \sim T_{\mathrm{CMBR}}$ (Johnson, 2011).

As the Jeans mass decreases in this type of environment, the stars formed under these circumstances would probably have lower characteristic masses

($M \sim 10M_\odot$) compared to the first pop III stars ($M \sim 100M_\odot$) (Greif & Bromm, 2006). It is therefore convenient to divide pop III stars into two subclasses. Pop III.1 stars formed first in minihalos, while the pop III.2 stars formed after some pop III.1 stars died and are hence affected by the radiation from these stars (Tan & McKee, 2008).

3.1 Initial mass functions

IMFs are usually described as power-laws:

$$\frac{dN}{dM} \propto M^{-\alpha}. \tag{3.7}$$

In 1955, Salpeter (1955) suggested that the value of α was 2.35 for stars heavier than one solar mass. This IMF is called a *Salpeter function*. This work was later extended by Kroupa (2001) who adopted $\alpha = 2.3$ for $M > 1M_\odot$ and other values for mass ranges under one solar mass. This type of mass function is called the *Kroupa IMF*. In this work we will consider the Kroupa IMF, a moderately top-heavy log-normal IMF as well as an extremely top-heavy IMF to account for different possible scenarios.

3.2 Black holes in the first galaxies

The stronger the Lyman-Werner radiation field is, the more inefficient the H_2-cooling becomes. According to simulations by Shang et al. (2010), if the flux of Lyman-Werner photons exceeds a critical value, the gas will be unable to cool sufficiently to form stars. Instead, the the material continues to fall onto the halo until it collapses under its own weight and forms a black hole. This black hole would probably exceed 10^4 $M_\odot$ (Shang et al., 2010).

It is possible that these black holes are the seeds of the supermassive black holes (SMBHs) observed today at $z \leq 6$ (Johnson, 2011).

If black holes are formed inside an atomic cooling halo, it would affect the properties of the gas. As material accretes around the black hole it releases potential energy and heats the gas. In the inner parts of the accretion disk the temperature can reach values of $T \approx 10^7$ K (Johnson, 2011). The high temperature suggests that the black holes formed by collapse in the atomic cooling halos emit large amounts of Lyman-Werner radiation, X-rays and ionizing radiation (Johnson, 2011).

3.3 The transition from pop III to pop II

As previously mentioned, pop III galaxies are characterized by zero-metallicity. But after the first supernovae explode, they will affect the surrounding medium. Stars formed in these environments will have different characteristics due to the enrichment of heavy elements from the supernova eruptions.

Stars with initial masses of 40-140 $M_\odot$ or > 260 $M_\odot$ will, at the end of their lives, form a black hole without a preceding explosion (Heger et al., 2003), and does not significantly change the chemical composition of the circumstellar medium (Greif et al., 2008a). Stars with $140M_\odot < M < 260M_\odot$ will, however, explode as pair instability supernovae (PISNe) (Heger et al., 2003). This type of supernova disrupts the entire star, i.e. leaving no remnant and the heavy elements created in its core are ejected into the primordial gas.

The energy released by the supernova causes the hosting halo to expand until the gas that has been chemically enriched starts to collapse again to form new stars (Johnson, 2011). The gas that collapses back into the halo has a characteristic metallicity of $\sim 10^{-3}$ $Z_\odot$ (Johnson, 2011), and the stars formed in this environment would have the same chemical composition, making them the first pop II stars.

The degree of the metal distribution is mostly determined by the energy released in the supernova explosion, which can be 10^{51-53} erg (Greif et al., 2007).

3.4 Lyman break galaxies

Photons from distant galaxies are affected on their way to an observer. Not only are they redshifted, but they can also be absorbed and re-emitted in intergalactic clouds in the line of sight. One of these effects is the *Lyman-α forest.* Neutral hydrogen in intergalactic space absorbs the Lyman-α photons and an absorption line appears in the observed spectrum. As clouds with neutral hydrogen can reside at any redshift, the resulting spectrum is a number of absorption lines at wavelengths shorter than the rest-wavelength $\lambda_{\mathrm{Ly}\alpha} = 1216$ Å, see Fig. 3.4. In this spectrum it is clear that at wavelengths shorter than 1216 Å , the flux is significantly reduced due to the Lyman-α forest.

For galaxies located at high redshifts (i.e. $z > 6$), the Lyman-α forest is so strong that all light at energies higher than 1216 Å is absorbed (Steidel et al., 1996). This will result in a spectrum with a "cut off" blue-ward of the Lyman-α line, and a galaxy like this is called a *Lyman break galaxy.*

The higher the redshift, the more the Lyman break moves to the red part of the spectrum; e.g. at a redshift of $z = 8$ the break would appear at $\lambda \approx 11000$ Å, i.e. in the infrared Y-band.

Galaxies which are visible in one filter but whose fluxes are significantly reduced or undetected in the bluer neighboring filter are usually referred to as drop-out galaxies.

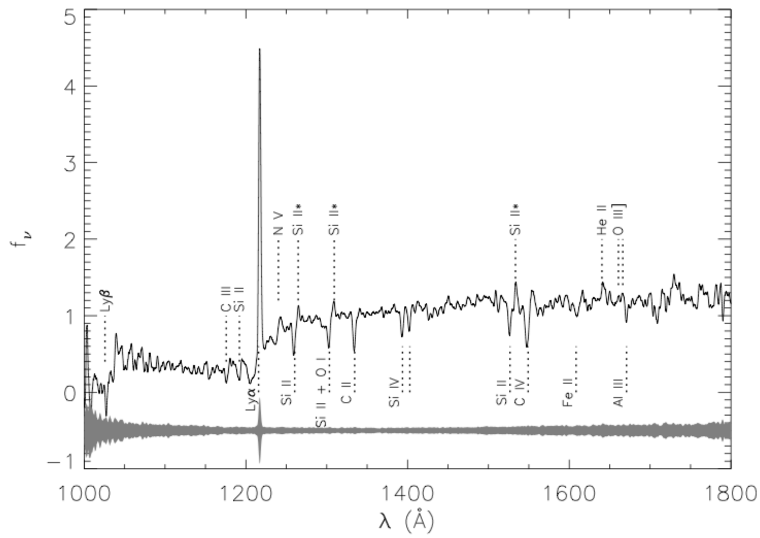

Figure 3.4: Composite spectrum of 81 galaxies in a sample with redshift range $3.5 < z < 4.5$. It is clear from this plot that radiation at wavelengths shorter than 1216 Å is significantly reduced due to the Lyman-α forest. Credit: Jones et al. (2011).

4 The Yggdrasil model

In order to detect pop III galaxies, we need a tool to predict their signatures based on their intrinsic conditions. This is where *Yggdrasil* comes in; this is a model used to predict e.g. the magnitudes in different filters for different stellar populations and galaxies.

As mentioned, we expect true pop III galaxies to form in regions that have not yet been chemically enriched. It is possible that there exist *hybrid galaxies*; these are galaxies that have an incomplete mixing of metals. Some regions of primordial gas remain their initial chemical composition (Zackrisson et al., 2011). The existence of these regions can be explained by e.g. a non-homogenous mass distribution. In this non-metallicity environment pop III stars can form, among with higher metallicity stars in the other parts of the galaxy.

Yggdrasil models the spectral energy distributions (SEDs) of galaxies with varying metallicity at high redshifts and takes into account e.g. nebular emission and dust extinction. As the IMF is uncertain for pop III galaxies, it is possible to alter between e.g. top-heavy IMFs and the Kroupa IMF which is adopted for pop I and II galaxies.

One of the assumptions going in to the code is that of a spherical nebula with a constant hydrogen density.

The presence of dust does not appear in the earliest stages in star formation at high redshift. However, stars with masses ranging between 140

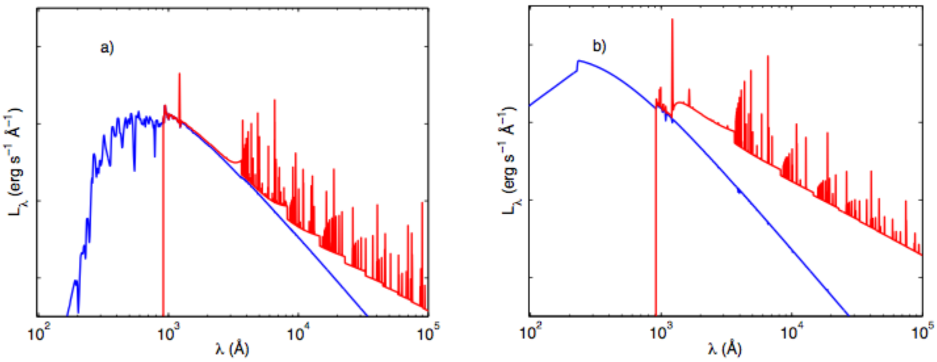

Figure 4.1: SEDs of two 1 Myr old dust-free galaxies. The left panel is the SED for a pop I galaxy with a metallicity of $Z = 0.02$ while the right panel represent a pop III.1 galaxy. The blue lines correspond to if the SEDs were dominated by the stellar emission and the red lines show the SED if both stellar and nebular effects are taken into account. Credit: Zackrisson et al. (2011).

and 260 $M_\odot$ end their lives as PISNe after a few million years (Heger et al., 2003), which will release dust that affects the overall spectra of galaxies.

4.1 Nebular contribution and dust

If the gas around a galaxy is photoionized, it will affect the SED. In Fig. 4.1 the difference is displayed for two types of galaxies. It is clear from these plots that the presence of a nebula around the galaxy significantly changes the shape of the spectrum.

The surrounding gas absorbs photons with shorter wavelengths than 912 Å(the Lyman limit) and this is why the red lines show a break at this wavelength.

The nebular contribution is determined by using the method described in Zackrisson et al. (2001). Model spectra for different types of stars, e.g. different metallicities, ages and masses are used to create template spectra for different types of stellar populations. In our current analysis, this is done using the *Starburst99* code (Leitherer et al., 1999) for pop I and pop II galaxies and Schaerer (2002) and Raiter et al. (2010) stellar population spectra for pop III galaxies. The output from these codes is then used as input to *Cloudy* (Ferland et al., 1998). This code generates spectra for stellar populations that are surrounded by nebulae.

The envelope of gas around the galaxy does not have to be homogenous; supernova effects or radiation may create holes in the nebula. This causes a leakage of star light that does not interact with the nebula, and hence altering the spectrum. This effect is governed by the *covering factor*, $f_{\rm cov}$, and ranges between 0 and 1. A value of $f_{\rm cov} = 1$ means that no direct star light reaches the observer; $f_{\rm cov} = 0$ would imply no surrounding nebula.

Another property that Cloudy takes into account is the fact that there may exist pockets of low-density-regions in the nebula. This is controlled by the *filling factor*, f_{fill} and it describes the porosity of the gas.

The parameters that are used as input to Yggdrasil is the nebula's inner radius, R_{in}, and the mass that is used to form new stars, M_{tot}. M_{tot} is simply estimated by integrating the star formation rate (SFR) over the duration of a star-forming episode:

$$M_{\text{tot}} = \int_0^\tau \text{SFR}(t)\, dt. \tag{4.1}$$

The inner radius is determined by using

$$R_{\text{in}} = 100\, R_\odot \left(\frac{L}{L_\odot}\right)^{1/2}, \tag{4.2}$$

where L is the bolometric luminosity (Zackrisson et al., 2011).

The mass used to form new stars is set to $M_{\text{tot}} = 10^6\, M_{\text{tot}}$, but our results are not that sensitive to this assumption. The colors one would receive by using the *James Webb Space Telescope* (*JWST*) would not change significantly even if this value would have been three orders of magnitude larger (Zackrisson et al., 2011).

After the first supernovae in the first galaxies explode, one has to take into account the extinction from dust. So called *attenuation laws* are then used in Yggdrasil (Pei, 1992; Calzetti, 1997). It is assumed that the dust is present outside the photoionized region: this is viable for young pop III galaxies since we do not expect any dust surrounding pop III stars (Zackrisson et al., 2011). For simplicity, we make the same assumption for pop I/II stars.

The nebular contribution to the SED is prominent for young pop III galaxies, as shown in Fig. 4.2. In the right panel the cyan line (pop III.1) ends at $\sim 10^{6.5}$ years; this is due to that pop III.1 stars generally do not live longer than this (Schaerer, 2002).

4.2 Type A, B and C

The impact of the surrounding gas can vary from different galaxies. It is therefore convenient to divide them into three classes:
Type A. This is the so-called ionization-bounded HII region. If an ionizing source is surrounded by nebular gas, the photons will ionize the gas. For smaller radii of the surrounding gas, the ionizing photons have a higher density and the state of ionization is larger. If the density of the nebular gas is high enough, it will absorb all the ionizing photons and it is called an ionization-bounded nebula. Any Lyman-continuum would be absorbed by the nebula and the nebular emission would dominate the SED of the galaxy.
Type B is an intermediate class where a part of the ionizing photons escape

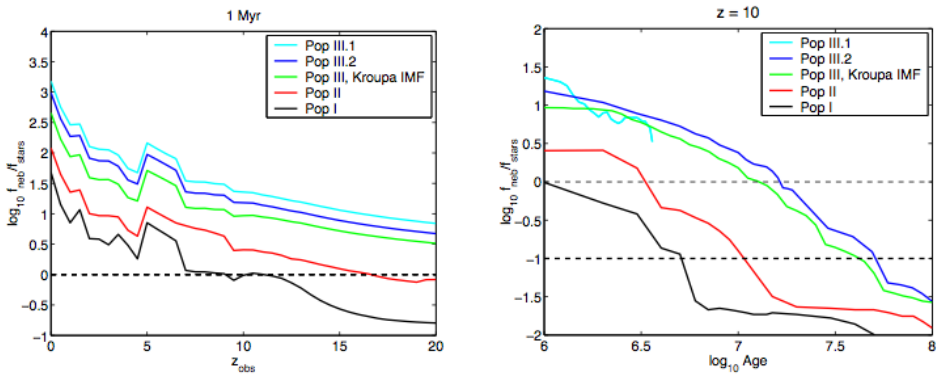

Figure 4.2: The left panel shows the nebular contribution in the F444W filter in a 1 Myr old as a function of redshift. The right plot displays the nebular contribution as a function of age at redshift $z = 10$. The black and red lines correspond to pop I and pop II galaxies respectively. The cyan line is a pop III.1 galaxy, the blue line is a pop III.2 galaxy and the green line represent a pop III galaxy with a Kroupa IMF. Credit: Zackrisson et al. (2011).

into the intergalactic medium.
Type C is the opposite of type A. Here, all the Lyman radiation escapes from the nebula and the nebular emission does not significantly affect the SED of the galaxy.

In Yggdrasil, only type A and C galaxies are taken into account; it would be more difficult to model the type B galaxies due to e.g. the time dependence of the gas density.

By setting f_{cov} between 0 and 1 it is possible to use this as a substitute for type B galaxies. However, even if the result may be a rough estimate of the SED from this type of galaxy it should be taken with caution since it is not a true simulation of a type B galaxy.

5 Gravitational lensing

Light that travels from a source to an observer is affected in different ways on its path. One of these effects is gravitational lensing; this is the bending of light when it passes a massive object. The deflection of light was first mentioned in 1804 by Johann Soldner, a german scientist (Wambsganss, 1998). In 1911, Albert Einstein published a paper about the gravity on light, but it was not until the advent of general relativity that he obtained the angle by which light is deflected:

$$\tilde{\alpha} = \frac{4GM}{c^2}\frac{1}{r}, \tag{5.1}$$

where c is the speed of light, G is the gravitational constant, r is the distance from the photon and the lens and M is the mass of the lens.

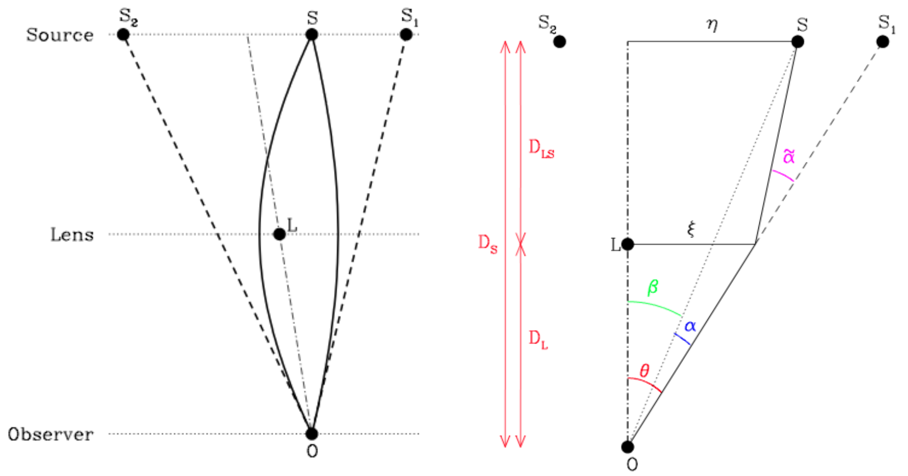

(a) (b)

Figure 5.1: The case of gravitational lensing. (a) The source S emits photons that are deflected by the lens L and the observer O sees two images, S_1 and S_2. (b) Definitions and relations between angles. Credit: Wambsganss (1998).

It is assumed that the thickness of the lens is so small that it can be neglected. This is referred to as the *thin lens approximation* and is valid for almost all cases in astronomy, where the distance between emitter and observer usually is significantly larger than the thickness of the lens (Wambsganss, 1998).

A Friedmann-Robertson-Walker metric is assumed:

$$ds^2 = \left(1 + \frac{2\Phi}{c^2}\right) c^2 dt^2 - a^2(t) \left(1 - \frac{2\Phi}{c^2}\right) d\sigma, \tag{5.2}$$

where Φ is the Newtonian potential and the left term is the perturbation caused by the lens.

In Fig. 5.1 schematic pictures of the lensing situation is shown. For gravitational lenses at cosmological distances, one has to consider e.g. the curvature of space-time. In this simplified case this is not taken into account.

From Fig. 5.1b we can se that the following relation is valid if all angles are very small, which is the case for gravitational lensing (Wambsganss, 1998):

$$\alpha D_{\mathrm{S}} = \tilde{\alpha} D_{\mathrm{LS}}. \tag{5.3}$$

Additionally, the relation between the angles θ, α and β is simply given by

$$\beta = \theta - \alpha(\theta), \tag{5.4}$$

and by applying this to Eq. 5.1 we obtain

$$\tilde{\alpha} = \frac{4GM(\xi)}{c^2}\frac{1}{\xi}, \tag{5.5}$$

where $M(\xi)$ is the mass inside radius ξ. By plugging Eq. (5.3) in to Eq. (5.4) we obtain

$$\beta = \theta - \frac{D_{\mathrm{S}}}{D_{\mathrm{LS}}}\tilde{\alpha}. \tag{5.6}$$

Now, we insert Eq. (5.5) and get

$$\beta = \theta - \frac{D_{\mathrm{LS}}}{D_{\mathrm{S}}}\frac{4GM}{c^2}\frac{1}{\xi}. \tag{5.7}$$

The final step is to use $\xi = D_{\mathrm{L}}\theta$ which can be seen from Fig. 5.1b. We then obtain

$$\beta = \theta - \frac{D_{\mathrm{LS}}}{D_{\mathrm{L}}D_{\mathrm{S}}}\frac{4GM}{c^2\theta}. \tag{5.8}$$

If the source is perfectly aligned with the lens in the line of sight a special phenomenon occurs. The light is equally affected in all directions and the observer sees an *Einstein ring*. In this case the angle β is zero and Eq. (5.8) simplifies and we can solve for θ,

$$\theta_{\mathrm{E}} = \sqrt{\frac{4GM}{c^2}\frac{D_{\mathrm{LS}}}{D_{\mathrm{L}}D_{\mathrm{S}}}}, \tag{5.9}$$

where θ_{E} is called the *Einstein radius*. This pehomenon is not often observed, but the concept is useful since θ_{E} can give an idea on how suitable a lens is as a magnifier.

5.1 Magnification

By considering Eq. (5.9) it is convenient to simplify Eq. (5.8):

$$\beta = \theta - \frac{\theta_{\mathrm{E}}^2}{\theta}. \tag{5.10}$$

By then solving for θ we obtain

$$\theta_{1,2} = \frac{1}{2}\left(\beta \pm \sqrt{\beta^2 + 4\theta_{\mathrm{E}}^2}\right). \tag{5.11}$$

The magnification of an object behind a lens is given by the ratio of the solid angles of the source and the picture that the observer sees, i. e.

$$\mu = \frac{\theta}{\beta}\frac{d\theta}{d\beta}, \tag{5.12}$$

and

$$\mu_{1,2} = \left(1 - \left(\frac{\theta_{\mathrm{E}}}{\theta_{1,2}}\right)\right)^{-1}. \tag{5.13}$$

If $\beta < \theta_{\mathrm{E}}$ i.e. the source is inside the Einstein radius it is mirrored. This is the case for a singular isothermal sphere (SIS). This the simplest description of the distribution of matter in systems in the universe e.g. galaxy clusters. The density distribution is described by

$$\rho(r) = \frac{\sigma_V^2}{2\pi G r^2}, \tag{5.14}$$

where σ_V^2 is the velocity dispersion. For other types of mass distributions, the resulting images could be more than one source.

As mentioned previously, if an object lies directly behind the lens, the observer will see an Einstein ring. However, if $\beta = 0$ in Eq. (5.12) the magnification goes to infinity. This is due to the simplifications made; for instance, the emitter is assumed to be a point source and the lens is assumed to be infinitely thin. By taking into account that a source usually is not point-like and allowing the lens to have a thickness, the magnification for an emitter directly behind a gravitational lens, is indeed finite.

5.2 Advantages and drawbacks

One of the main advantages of gravitational lensing is that of not having to expose the field of view for so long, as is the case for Ultra Deep Fields (UDFs). As the lenses increase the flux from a background source it is possible to detect objects that are too faint for the UDFs. Two other factors work in its favor. First, not only is the flux of the source enhanced; the observed size is also magnified, allowing more detailed studies of the structure. Second, the fact that some of the objects will appear with more than one image, allows astronomers to separate them from spurious objects (Bradač et al., 2009).

A drawback for gravitational lensing is that even if the fluxes of the lensed sources are amplified, the area of the source plane is reduced by a factor μ. As a result of this, a smaller volume at high redshift is examined, compared to an un-lensed field.

5.2.1 Galaxy clusters as gravitational lenses

The fact that clusters of galaxies are very massive makes them excellent tools for observing the distant universe; the number of high-redshift candidates is significantly higher compared to an un-lensed field. In fact, a large fraction of all $m < 25.5$(AB) galaxies at $z \gtrsim 6.5$ have been detected using galaxy clusters as cosmic telescopes (Postman et al., 2012).

Additionally, examining a cluster that works as a gravitational lens provide an excellent way of mapping the dark matter distribution in that cluster.

The magnification from a cluster can range between $\mu = 10 - 100$ (Maizy et al., 2010).

6 CLASH

The Cluster Lensing And Supernova survey with Hubble (CLASH) is a program that targets 25 galaxy clusters and will observe them in 16 filters.

There are four main goals for CLASH (Postman et al., 2012):

1. Estimate the dark matter distribution in galaxy clusters more accurately than in prevoius surveys.

2. Explore e.g. the time dependent equation of state in high redshift ($z \sim 2.5$) supernovae.

3. Find high redshift ($z \sim 7$) galaxies and determine their properties.

4. Examine galaxies in and behind the targeted clusters.

6.1 The cluster sample

There have been minor surveys prior to CLASH, containing 5-10 clusters. However, these clusters were selected only due to their suitability as gravitational lenses (Postman et al., 2012). This causes the sample to become biased towards clusters with a higher central mass concentration. To avoid this, 20 clusters selected for CLASH are mainly chosen using X-ray observations to make sure that they are dynamically relaxed. The remaining five are selected based on their large Einstein radius ($\theta_{\mathrm{E}} > 35''$). For the study carried out in this thesis, the high magnification clusters are of the largest interest. The large value on the Einstein radius increases the area with large μ.

The reasons for using data from CLASH are the facts that the catalogs contain a large amount of data and the clusters are observed in many filters.

The mass range of all the clusters is relatively large ($\sim 5 - 30 \cdot 10^{14} M_{\odot}$) and the redshifts lie between $z_{\mathrm{min}} = 0.18$ and $z_{\mathrm{max}} = 0.90$. See Table 1 for details on the full sample.

6.2 The project design

The 16 filters that will be used for the survey range between 2000 and 17000 Å; this corresponds to near-ultraviolet to near-infrared (Postman et al., 2012). The instruments that are being used for the study are the Advanced Camera for Surveys (ACS) and the Wide Field Camera 3 (WFC3) onboard

Cluster	α_{J2000}	δ_{J2000}	z_{Clus}
X-ray selected clusters			
Abell 209	01:31:52.57	-13:36:38.8	0.206
Abell 383	02:48:03.36	-03:31:44.7	0.187
MACS0329.7-0211	03:29:41.68	-02:11:47.7	0.450
MACS0429.6-0253	04:29:36.10	-02:53:08.0	0.399
MACS0744.9+3927	07:44:52.80	+39:27:24.4	0.686
Abell 611	08:00:56.83	+36:03:24.1	0.288
MACS1115.9+0129	11:15:52.05	+01:29:56.6	0.352
Abell 1423	11:57:17.26	+33:36:37.4	0.213
MACS1206.2-0847	12:06:12.28	-08:48:02.4	0.440
CLJ1226.9+3332	12:26:58.37	+33:32:47.4	0.890
MACS1311.0-0310	13:11:01.67	-03:10:39.5	0.494
RXJ1347.5-1145	13:47:30.59	-11:45:10.1	0.451
MACS1423.8+2404	14:23:47.76	+24:04:40.5	0.545
RXJ1532.9+3021	15:32:53.78	+30:20:58.7	0.345
MACS1720.3+3536	17:20:16.95	+35:36:23.6	0.391
Abell 2261	17:22:27.25	+32:07:58.6	0.224
MACS1931.8-2635	19:31:49.66	-26:34:34.0	0.352
RXJ2129.7+0005	21:29:39.94	+00:05:18.8	0.234
MS2137-2353	21:40:15.18	-23:39:40.7	0.313
RXJ2248.7-4431 (Abell 1063S)	22:48:44.29	-44:31:48.4	0.348
High magnification clusters			
MACS0416.1-2403	04:16:09.39	-24:04:03.9	0.42
MACS0647.8+7015	06:47:50.03	+70:14:49.7	0.584
MACS0717.5+3745	07:17:31.65	+37:45:18.5	0.548
MACS1149.6+2223	11:49:35:86	+22:23:55.0	0.544
MACS2129.4-0741	21:29:26.06	-07:41:28.8	0.570

Table 1: The galaxy clusters in the CLASH sample. Credit: Postman et al. (2012).

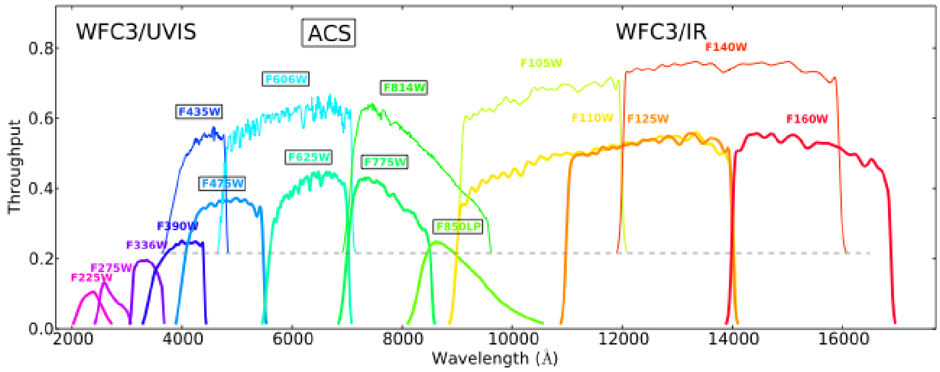

Figure 6.1: The CLASH filters. Some of the filters are plotted with a vertical offset of 0.2 to avoid the figure being to cluttered. Credit: Postman et al. (2012).

the Hubble Space Telescope (HST). In Fig. 6.1, all filter profiles available for CLASH are shown.

ACS will observe in the optical filters, while WFC3 will observe in the rest.

7 Results

The ability to predict the colors of pop III galaxies is crucial to be able to find suitable candidates. However, it is equally important to find the corresponding colors for other types of galaxies at the same redshift. This enables us to distinguish the pop III galaxies from mundane objects. Therefore, a variety of input parameters and combinations are used in the Yggdrasil model. The parameters used for this survey are f_{cov}, $f_{\mathrm{Ly}\alpha}$ and IMF. All stars in the galaxy types are assumed to have formed at one time, i.e. an instantaneous burst.

As pop III galaxies are expected to occur at high redshift, the Lyman break should appear in the IR or NIR. Hence, it is therefore filters in this wavelength range that are the interest of this survey.

7.1 Finding the characteristics

Fig. 7.1a shows how the colors of a young pop III galaxy evolves at $z = 7$. By plotting the tracks for different types of galaxies with different conditions it is possible to define a unique area in a color-color diagram that only harbors pop III galaxies at high redshifts.

Yggdrasil allows us to derive the colors for different redshifts and find out how they behave for different z; in Fig. 7.1b this is shown.

As a second step, we want to find the corresponding area for other types of galaxies to be able to generate a unique surface in the color-color plane which

Camera	Filter	10σ limit (AB mag)	5σ limit (AB mag)
WFC3	F225W	25.7	26.4
WFC3	F275W	25.7	26.5
WFC3	F336W	25.9	26.6
WFC3	F390W	26.5	27.2
ACS	F435W	26.4	27.2
ACS	F475W	26.8	27.6
ACS	F606W	26.9	27.6
ACS	F625W	26.4	27.2
ACS	F775W	26.2	27.0
ACS	F814W	27.0	27.7
ACS	F850LP	26.0	26.7
WFC3	F105W	26.6	27.3
WFC3	F110W	27.0	27.8
WFC3	F125W	26.5	27.2
WFC3	F140W	26.7	27.4
WFC3	F160W	26.7	27.5

Table 2: The filters used in CLASH with their limiting magnitudes. Credit: Postman et al. (2012).

is exclusive for pop III galaxies. Yggdrasil also offers evolutionary tracks for more chemically enhanced populations; in Fig. 7.2, the color evolution for a pop III galaxy along with corresponding tracks for pop I and II galaxies are shown. From this plot, it is clear that it seems to exist a part in the color-color plane that exclusively harbor pop III galaxies. Completing this figure with tracks for $6 < z < 9$ enables us to find a unique area exclusively for pop III galaxies at these redshifts.

This machinery enables us to generate two color-color surfaces using 4 filters. These are displayed in Fig. 7.3. As the different areas are generated using different filters, they also correspond to different redshifts. The left plot in Fig. 7.3a represent the redshift range $7 < z < 9$ while the right surface spans between $z = 6.5$ to $z = 8$.

In some surveys, however, another Y-filter is used. It is the narrower Y_{098}-filter which spans from $\sim 900 - 1100$Å, while Y_{105} has a wavelength range between ~ 900 and ~ 1200Å. In order to use data from studies using this filter, additional color criteria must be generated, as a pop III-patch would have a different appearance with a narrower filter. The method for obtaining these conditions is the same as previously described. In Fig. 7.3 the color criteria for the redshift intervals $6 < z < 7.7$ (Fig. 7.3a) and $7.5 < z < 9$ (Fig. 7.3b) are presented.

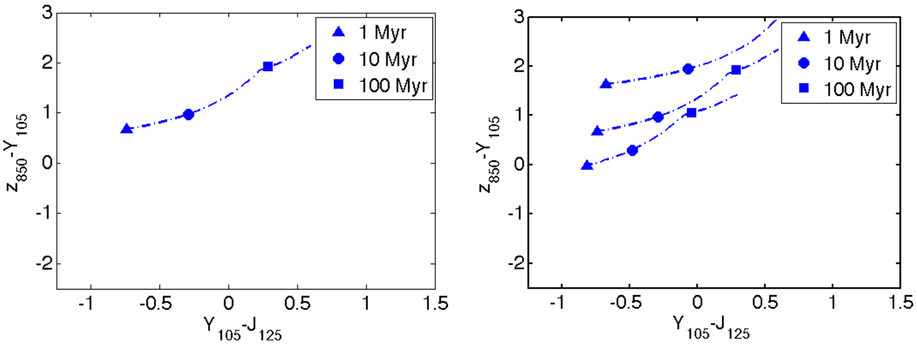

(a) (b)

Figure 7.1: (a) Evolutionary track of the colors $z_{850} - Y_{105}$ against $Y_{105} - J_{125}$ for a pop III galaxy with a Krupa IMF at redshift $z = 7$ with $f_{\rm cov} = 1$ and $f_{\rm Ly\alpha}$=0.5. It is assumed that all stars in the galaxy are formed at the same time, i.e. an instantaneous burst. The square, circle and triangle represent the different ages of the galaxy as described in the legends. As is clear from this plot, the galaxy becomes redder as it gets older. (b) Evolutionary tracks for the same type of galaxy as in the left panel. Here tracks for more than one redshift are displayed; from the bottom: $z = 6.5$, $z = 7$ and $z = 7.5$.

Apart from the pop III galaxy color signatures obtained from Yggdrasil, the dropout criteria from Bouwens et al. (2011), Eqs. (7.1), (7.2) and (7.4), are displayed for comparison. However, in the left panel in Fig. 7.3b the dropout criteria from Wilkins et al. (2011), Eqs. (7.12), are plotted. The reason is that in Bouwens et al. (2011), they are using $z - J$ to identify z-band dropouts, Eq. (7.3b), and in this study we will not be using those colors.

7.2 Ultra Deep Fields

The first objects to examine are samples from published articles which have distinguished a number of high redshift galaxies. The colors of these objects are used in the color-color planes obtained from Yggdrasil. In Fig. 7.4, we present all high-redshift sources from the UDFs that are used in this project. They are divided into Y-band dropouts and z-band dropouts.

In the following subsections, we will discuss all articles and candidates separately.

7.2.1 Bouwens et al. (2011)

The data set for this article is obtained by using ultra deep observations made with WFC3 and ACS over a two-year period. The sample is extended with data from GOODS (The Great Observatories Origins Deep Survey).

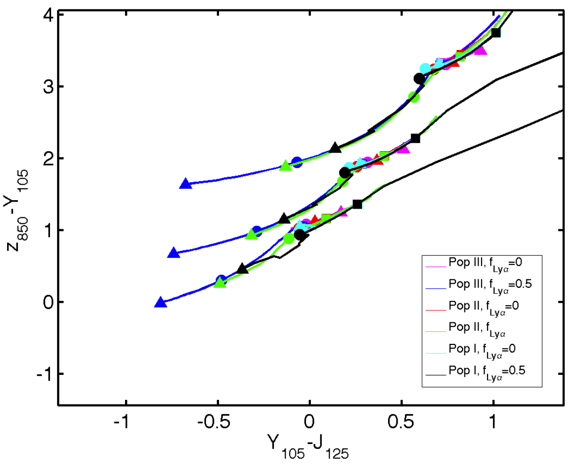

Figure 7.2: Evolutionary tracks ($z = 6.5$, $z = 7$ and $z = 7.5$) for different types of galaxies. The colors are explained in the legend. The circles, triangles and squares correspond to the same ages as explained in Fig. 7.1.

This is taken from the ERS (Early Release Science) observations; however, the Y-filter (Y_{098}) is different from the one used in WFC3 (Y_{105}).

To distinguish high-redshift galaxies from nearby objects Bouwens et al. (2011) make use of the signatures from Lyman break galaxies (Sect. 3.4) and the criteria:

$$(z_{850} - Y_{105} > 0.7) \wedge (Y_{105} - J_{125} < 0.45) \tag{7.1a}$$

$$\wedge\, (z_{850} - Y_{105} > 1.4(J_{125} - H_{160}) + 0.42), \tag{7.1b}$$

for z_{850}-dropouts and

$$(Y_{105} - J_{125} > 0.45) \wedge (J_{125} - H_{160} < 0.5), \tag{7.2}$$

for Y_{105}-dropouts. Corresponding criteria for the ERS-field are

$$z_{850} - J_{125} > 0.8 + 1.1(J_{125} - H_{160}) \tag{7.3a}$$

$$\wedge\, z_{850} - J_{125} > 0.4 + 1.1(Y_{098} - J_{125}), \tag{7.3b}$$

for z_{850}-dropouts and

$$Y_{098} - J_{125} > 1.25 \wedge J_{125} - H_{160} < 0.5, \tag{7.4}$$

for Y_{098}-dropouts. These conditions strongly favor star forming galaxies at $z \sim 7$ and $z \sim 8$. Another requirement is that the sources are detected with 4.5σ significance in the relevant filters. Furthermore, sources detected in optical bands are rejected since the Lyman-α forest should suppress the flux at these wavelengths.

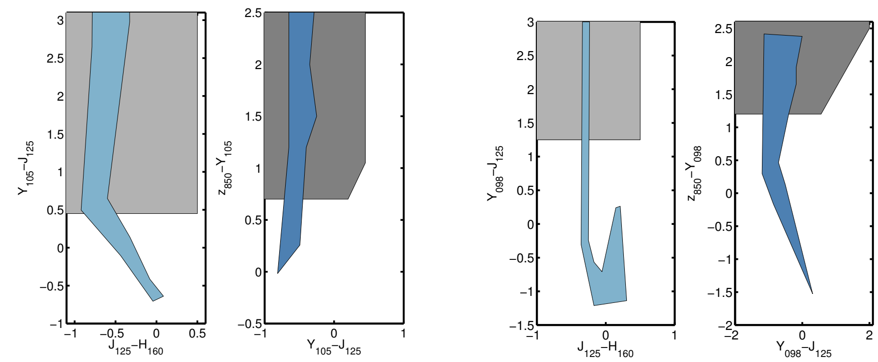

(a) (b)

Figure 7.3: (a) The areas corresponding to pop III galaxy signatures using filters z_{850}, Y_{105}, J_{125} and H_{160} (Blue regions). The grey regions correspond to the dropout criteria adopted by Bouwens et al. (2011). (b) The areas corresponding to pop III galaxy signatures using the filters z_{850}, Y_{098}, J_{125} and H_{160} (Blue patches). The grey area in the left panel correspond to the dropout criteria from Bouwens et al. (2011) and the grey area in the right panel corresponds to the dropout criteria adopted by Wilkins et al. (2011).

To further constrain the sample, Bouwens et al. (2011) use their $\chi^2_{\rm opt}$-method to exclude any low redshifts contaminants. For all optical data they generate a collective value of $\chi^2_{\rm opt}$ from the optical filters:

$$\chi^2_{\rm opt} = \sum_i \mathrm{SGN}(f_i)(f_i/\sigma_i)^2, \quad (7.5)$$

where f_i is the flux in filter i, σ_i is the uncertainty in the flux in band i and $\mathrm{SGN}(f_i)$ is 1 if $f_i > 0$ and -1 if $f_i < 0$. All objects exceeding a critical value of $\chi^2_{\rm opt}$ are rejected. This value is determined by simulations carried out by Bouwens et al. (2011).

Through tests and simulations, Bouwens et al. (2011) came to the conclusion that possible contaminants in their high-redshift sample are most likely low-redshift objects that are included due to photometric scatter. This effect has greatest impact for faint sources. The uncertainties associated to these objects are relatively large and this causes them to scatter in a color-color diagram. Additionally, the large number of faint sources further increases the risk of them entering the "high-redshift domain".

The technique of constraining the sample described above have led to an estimated contamination fraction of 11% (Bouwens et al., 2011).

The data used from the article includes $z_{850}-Y_{105}$, $z_{850}-Y_{098}$, $Y_{105}-J_{125}$, $Y_{098}-J_{125}$ and $J_{125}-H_{160}$ with their respective uncertainties. In Fig. 7.5a the colors from the $z \sim 7$ sample, i.e. z_{850}-dropouts, are displayed. As is clear in these plots, 7 candidates satisfy our color criteria in the $Y_{105} - J_{125}$

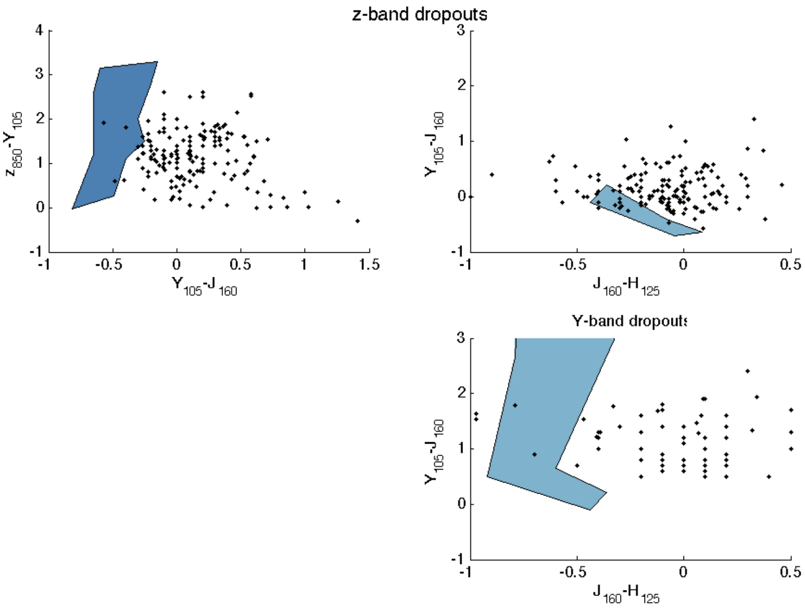

Figure 7.4: All candidates from the UDFs in the articles. The regions in the two figures at the top correspond to are $6 < z < 8$ and the lower figure corresponds to $8 < z < 9$.

vs. $J_{125} - H_{160}$ plane and no candidates in the $z_{850} - Y_{105}$ vs. $Y_{105} - J_{125}$ plane. The candidates in the left panel of Fig. 7.5a are plotted with their respective uncertainties in Fig. 7.5b.

The candidates meet our criteria in one color plane, but not the other. As we want as strong candidates as possible, we want them satisfy the conditions both planes, or be classified as candidates in more than one sample. As, these sources do are not detected in other data sets, we will not include them in the final sample.

By definition, Y_{105}-dropouts are not detected in the z_{850}-filter. Therefore, only the left panel in Fig. 7.3a can be used for these objects. In Fig. 7.6 it is clear that one of the objects in this sample met our color criteria; this is UDFy-39106493 (their notation). This pop III candidate is located at RA 03:32:39.10 and Dec -27:46:49.3. According to Bouwens et al. (2011) it has a redshift of $z \sim 8$ as it matches their Y-band dropout criteria.

This paper also contains small number of sources detected in the GOODS field. We then have to use the pop III signatures given in Fig. 7.3b. These results are presented in Fig. 7.7. None of the objects in the Y_{098}-dropout sample satisfied our color criteria for pop III galaxies.

The sources that met our criteria are ERSz-2160041591 and ERSz-2111644168 (their notation). They are located at RA 03:32:16.00, Dec -27:41:59.1 and RA 03:32:29.53, Dec -27:42:04.4, respectively. These objects

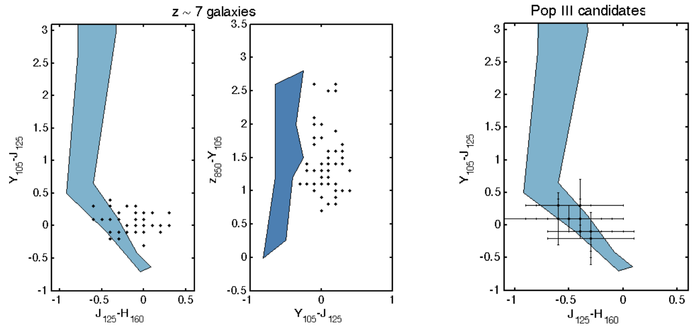

Figure 7.5: (a) The colors $Y_{105} - J_{125}$, $J_{125} - H_{160}$ and $z_{850} - Y_{105}$ from the z_{850}-dropout sample in Bouwens et al. (2011) in color-color diagrams. (b) Pop III candidates.

are not detected in any other sample, nor do they satisfy the color criteria in the $z - Y$ vs. $Y - J$ color plane. This does not make them unsuitable candidates; they are however not as convincing as the other sources in our final sample. ERSz-2160041591, ERSz-2111644168 and UDFy-39106493 are therefore not included in the final sample.

7.2.2 McLure et al. (2011)

This paper contains a sample of high-redshift galaxies obtained from the HUDFs (Hubble Ultra Deep Fields) and GOODS. The procedure of selecting high-redshift sources is different compared to Bouwens et al. (2011). The first step is to use a set of parameters in SExtractor (Source Extractor, a program designed to find sources in an image using pixel counts) to ensure detection in all relevant filters. Second, the uncertainties in the photometry were estimated. Third, by using a code to fit the SEDs, it was possible to estimate the photometric redshift of all the candidates. This code takes into account e.g. star formation rate, dust reddening, metallicity and age. A more detailed description of this code is found in McLure et al. (2011).

The first crude high-redshift catalog was obtained by only using sources who statistically satisfied a photometric redshift exceeding $z = 4.5$. This step excluded more than 90% of the original objects. The remaining sample was then examined to reject all objects whose high-redshift signatures could be explained by e.g. diffraction spikes.

To test the quality of the SED fits, the χ^2-method was used. The final sample of sources was then obtained by retaining only those objects with SED solutions which favored $z_{\text{phot}} \geq 6.0$. Additionally, the secondary redshift solution at lower z had to be excluded with at least 95% confidence. The final criterion was that the integrated probability function exceeded 0.5 for

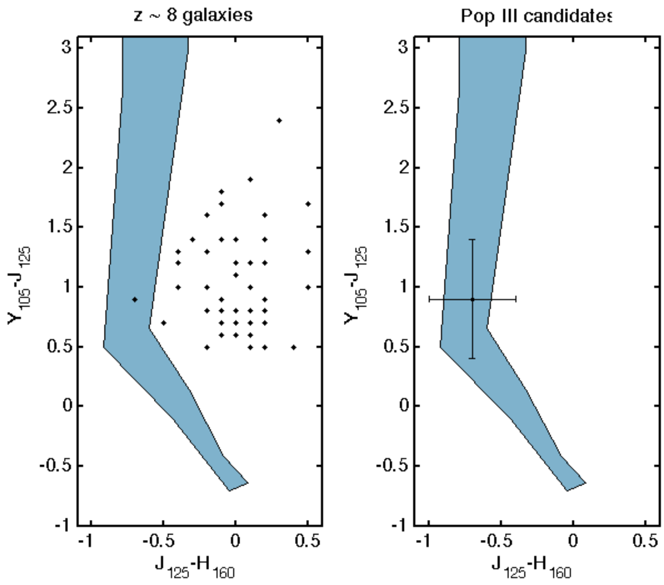

Figure 7.6: Objects in the $z \sim 8$ sample from Bouwens et al. (2011).

the redshift interval $6 \leq z \leq 10$, i.e.:

$$\int_{z=6}^{z=10} P(z')\delta z' \geq 0.5. \tag{7.6}$$

This strict approach of constraining the sample probably leads to true high-redshift objects being rejected. However, it decreases the risk of including low-redshift interlopers, hence it ensures a relatively clean catalog. The result is a sample of 70 sources ranging from $z = 6.0$ to $z = 8.7$.

In Fig. 7.8 the results from the UDF-catalog in McLure et al. (2011) are presented. It is clear from these plots that there is one candidate which satisfy our criteria for both color-color planes (HUDF_2836). In Fig. 7.9 the objects from the GOODS field are plotted. In this sample, another candidate met the criteria for our pop III galaxy signatures (ERS_9923). Both of these objects are presented in Fig. 7.10.

HUDF_2836

This candidate is located at RA 03:32:35.05 and Dec -27:47:25.8. The photometric redshift that McLure et al. (2011) estimates for this object is between $z = 5.97$ and $z = 6.43$, while the secondary redshift obtained from the χ^2-method is $z \sim 2$. It was possible to add Lyman-α radiation as a free parameter in the redshift fitting. By doing this, it was possible to obtain an alternative redshift where Lyman-α radiation is taken into account. This value reaches $z_{\mathrm{Ly}\alpha} = 6.51$ for this candidate.

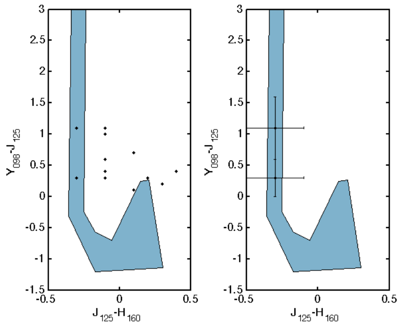

Figure 7.7: Left: All sources from the ERS-field from Bouwens et al. (2011). Right: The objects that met our color criteria.

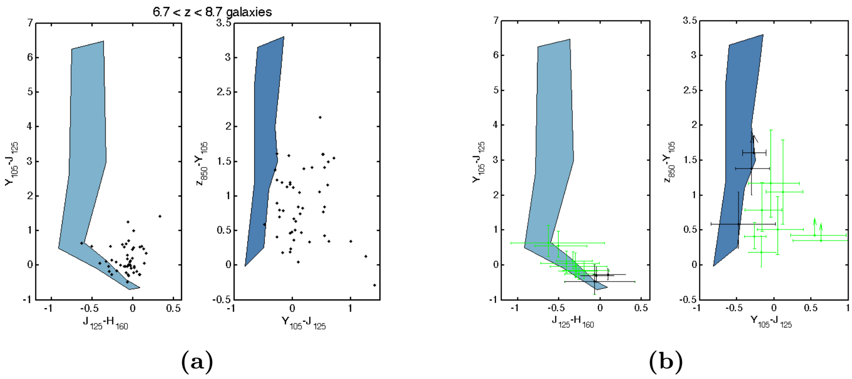

Figure 7.8: (a) Color signatures the UDF-catalog in McLure et al. (2011) (b) Candidates in McLure et al. (2011) that satisfy our pop III galaxy candidate criteria. Green data points represent sources that meet the criteria in the $Y_{105} - J_{125}$ vs. $J_{125} - H_{160}$ color-color plane. Black data points correspond to objects that satisfy our criteria in the $z_{850} - Y_{105}$ vs. $Y_{105} - J_{125}$ plane.

The apparent magnitude for this object is $m = 28.44$ in the Y_{105}-filter which makes it viable candidate for follow-up spectroscopy with e.g. *JWST*.

ERS_9923

At RA 03:32:10.06 and Dec -27:47:22.6 this object is our best pop III galaxy candidate so far. The photometric redshift without taking into account Lyman-α radiation is 6.59. However, by adding it as a free parameter this value increases to $z_{\mathrm{Ly}\alpha} = 7.59$. In fact, this candidate only classifies as a $z \geq 6$ object if Lyman-α is included in the fitting of the SED.

The best fit from Yggdrasil is a pop III.1 or pop III.2 galaxy with $f_{\mathrm{cov}} = 0.5$ and $f_{\mathrm{esc}} = 0.3$ at $z \approx 7.6$, which coincides with the value estimated by McLure et al. (2011). The magnitude for this candidate is $26.82^{+0.20}_{-0.17}$ in the

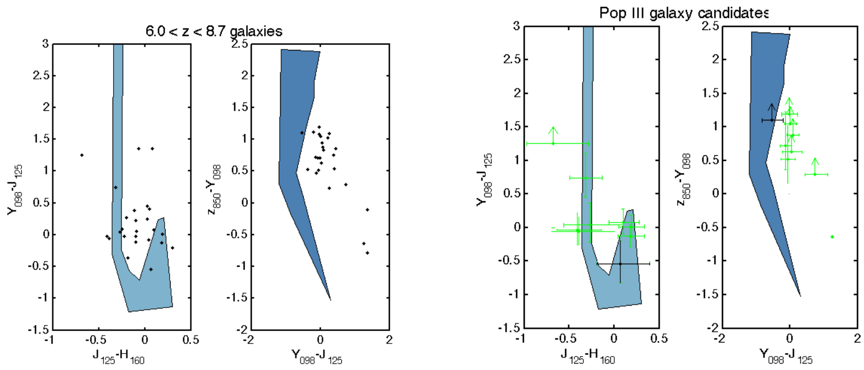

(a) (b)

Figure 7.9: (a) Color signatures the ERS-catalog in McLure et al. (2011) (b) Candidates in McLure et al. (2011) that satisfy our pop III galaxy candidate criteria. Green data points represent sources that meet the criteria in the $Y_{098} - J_{125}$ vs. $J_{125} - H_{160}$ color-color plane. Black data points correspond to objects that satisfy our criteria in the $z_{850} - Y_{098}$ vs. $Y_{098} - J_{125}$ plane.

Y_{098}-band. This relatively bright object makes it possible to observe and perform spectroscopy.

HUDF_2324

In the sample from McLure et al. (2011), two objects met our color criteria in both planes. However, by examining the coordinates of each object, it was uncovered that the samples from the different articles treated in this study can overlap. This is the case for HUDF_2324 in this sample; it corresponds to UDFz-42406242 in Bouwens et al. (2011). This object is located at RA 03:32:35.05 and Dec -27:47:25.8. The fact that it is included in different samples with different criteria and still satisfies our color conditions makes it a strong pop III candidate. McLure et al. (2011) estimates the redshift of this candidate to $6.18 < z < 6.60$ while it enters the $z \sim 7$ regime in Bouwens et al. (2011).

The brightness for this objects is estimated to $m_{\rm J} = 28.1 \pm 0.1$ in Bouwens et al. (2011) and $m_{\rm J} = 28.55^{+0.20}_{-0.17}$ in McLure et al. (2011).

7.2.3 Lorenzoni et al. (2011)

The high-redshift candidates from this paper are obtained by using the Lyman break technique. As this article concentrates on galaxies at $z \approx 8 - 9$ where the break occurs at $\lambda \sim 11000$Å, they are collecting objects that show a significant flux reduction in between $Y_{105/098}$ and J_{125} from both UDFs and the ERS-field. The detection thresholds was set to 2σ.

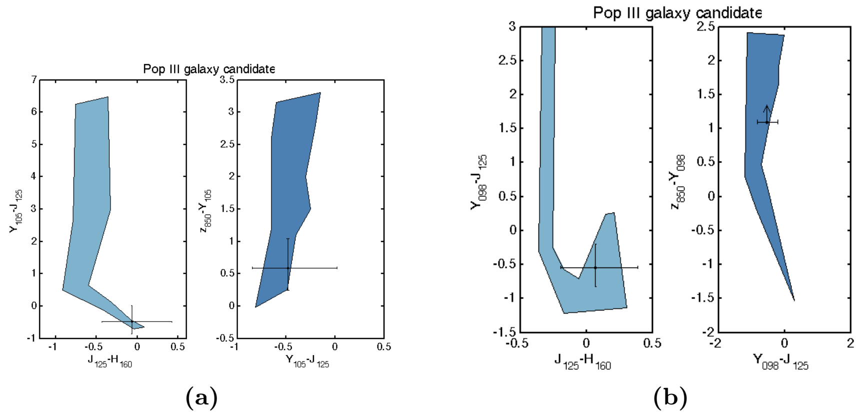

Figure 7.10: (a) The pop III candidate HUDF_2836. (b) The pop III candidate ERS_9923 located in the GOODS field.

To exclude possible low-redshift contaminants Lorenzoni et al. (2011) adopt color criteria which favor higher redshift galaxies:

$$(Y_{105} - J_{125}) > 0.9 \tag{7.7a}$$
$$(Y_{105} - J_{125}) > 0.73(J_{125} - H_{160}) + 0.9 \tag{7.7b}$$
$$(J_{125} - H_{160}) < 1.5, \tag{7.7c}$$

for the HUDF-fields and

$$(Y_{098} - J_{125}) > 0.9 \tag{7.8a}$$
$$(Y_{098} - J_{125}) > 0.64(J_{125} - H_{160}) + 1.28 \tag{7.8b}$$
$$(J_{125} - H_{160}) < 0.8. \tag{7.8c}$$

To exclude as many of the possible low-redshifts contaminants that have entered the sample due to photometric scatter, Lorenzoni et al. (2011) put a non-detection constraint in b_{435}, v_{606} and i_{775}. Objects with $> 2\sigma$ detection in any of these filters were rejected.

In Fig. 7.11, the results from both the UDFs and ERS-fields are presented. As all objects are selected using in Eqs. 7.7 and 7.8, we can only use our color-criteria for the $Y - J$ and $J - H$ plane.

Fig. 7.11 shows that there are some objects that end up to the left of our color criteria. These could be objects with extreme Lyman-α radiation as is not likely that pop I/II galaxies have that extreme colors (Zackrisson et al., 2011) . Therefore, these objects are considered pop III galaxy candidates. However, some of these extraordinary objects have extreme uncertainties, and are therefore excluded from subsequent analysis. In the UDFs this concerns P12.YD1 whose H-band magnitude was impossible to determine due

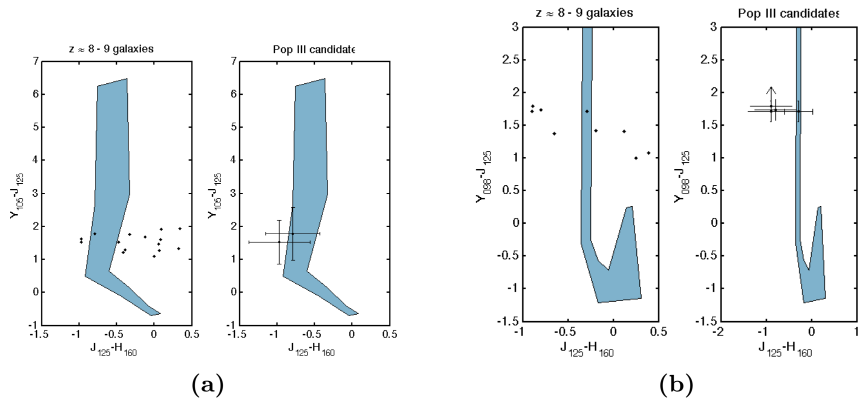

Figure 7.11: The results from Lorenzoni et al. (2011). (a) Left: All objects in the HUDFs. Right: Possible pop III galaxies with their respective uncertainties. (b) All galaxies in the ERS-field. Right: Objects of interest with their error estimates.

to the short exposure time (Lorenzoni et al., 2011). In the ERS field this is ERS.YD5 who only meet the color criteria from Lorenzoni et al. (2011) if they only required 1σ detection.

ERS_9041

One of the objects that occur to the left of the surface in Fig. 7.11b also appears in the sample generated by McLure et al. (2011). In this diagram the object appear to the left of the highlighted area, which could be indicative a strong Lyman-α radiation. In McLure et al. (2011) it is called ERS_9041 while in Lorenzoni et al. (2011) it is called ERS.YD1.

The source is located at RA 03:32:23.37 and Dec -27:43:26.5 and its magnitude in the J_{125}-filter is $27.23^{+0.10}_{-0.09}$. The most likely redshift according to McLure et al. (2011) is $7.61 < z < 8.20$. By taking into account Lyman-α radiation the best SED fit gives $z_{\mathrm{Ly}\alpha} = 8.16$.

In fact, this candidate is so strong that a proposal for observing this object will be submitted to ESO (European Southern Observatory).

7.2.4 Finkelstein et al. (2010)

This paper uses observations made by WFC3, ACS and *Spitzer*. Only objects with $> 2\sigma$ detection in relevant filters were included in the sample. For each object they determined the photometric redshift using the χ^2-method. From this value it was possible to estimate the probability distribution function,

$$P(z) \propto \exp(-\chi^2/2), \tag{7.9}$$

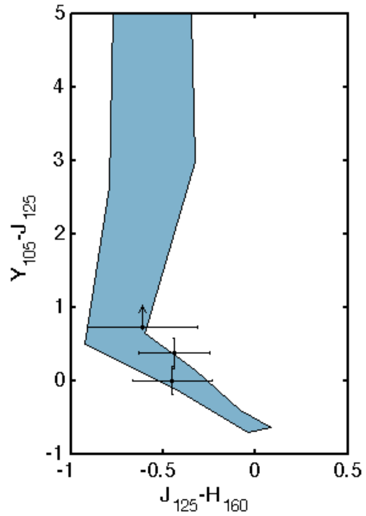

Figure 7.12: Three candidates that met our color criteria in Finkelstein et al. (2010).

where $\int_0^\infty P(z) = 1$. Objects that did not satisfy

$$\int_6^{11} P(z)dz > 0.6 \tag{7.10}$$

were excluded from the sample. In contrast to most other papers, Finkelstein et al. (2010) do not use any color criteria based on the Lyman break or apply non-detection constraints in the i_{775} or z_{850} band. Instead, they are confident that using all available filters (b_{435}, v_{606}, i_{775}, z_{850}, Y_{105}, J_{125} and H_{160}) to determine the photometric redshift will ensure a clean sample. Indeed, all galaxies in the sample show no detection in b_{435}, v_{606} or i_{775} with signal-to-noise ratio greater that 2 in all but one object. However, this could be explained by a nearby galaxy that affects the magnitude in the i_{775}-band. Additionally, all objects harbor the significative Lyman break feature in both $z_{850} - Y_{105}$ and $Y_{105} - J_{125}$ colors.

In Fig. 7.12 the results from this paper is presented.

Three of the objects satisfied our color criteria; 1445, 2013 and 653 (their notation). As is the case with ERSz- 2160041591 and ERSz-2111644168 in Bouwens et al. (2011), these candidates do not appear within the color criteria in any other sample, and will therefore not be included in the final sample of this project.

7.2.5 Wilkins et al. (2011)

The authors of this paper make use of observations made by both ACS/WFC3 and GOODS. The first constraint they adopt for their sample is a J_{125} magnitude cut. The reason for choosing this filter is that at $z \approx 7$ this band shows no signatures of a Lyman break or Lyman-α radiation. The authors are interested in determining the rest-frame ultra-violet luminosity. A filter that is not contaminated by emission lines or any other features is therefore desirable. At the same time, they want the signal to be as strong as possible in this filter. Objects in the sample are therefore required to have a 7σ detection in J_{125}.

As many other surveys, the procedure to select high-redshift galaxies are based on the colors of the objects. In this particular paper, the criteria are

$$(z_{850} - Y_{105}) > 1.0 \tag{7.11a}$$
$$(z_{850} - Y_{105}) > 2.4(Y_{105} - J_{125}) + 0.4 \tag{7.11b}$$
$$(Y_{105} - J_{125}) < 1.0, \tag{7.11c}$$

for the Hubble data and

$$(z_{850} - Y_{098}) > 1.2 \tag{7.12a}$$
$$(z_{850} - Y_{098}) > 0.9(Y_{098} - J_{125}) + 0.7 \tag{7.12b}$$
$$(Y_{098} - J_{125}) < 2.0, \tag{7.12c}$$

for the GOODS field. They emphasize that these constraints favor objects with a red UV spectral slope which could indicate the presence of dust.

Through simulations, Wilkins et al. (2011) conclude that the contamination fraction of the final sample is $\sim 5\%$ and these contaminants enter the sample most likely through photometric scatter. They also explore the possibility of objects being transient, e.g. supernovae. The images were inspected and one candidate was removed due to the suspicion of being such an object. This resulted in a final sample of 34 objects in the Hubble data and 11 candidates in the GOODS field.

After processing the sample from Wilkins et al. (2011), a number of objects were found that matched our color criteria. However, they are not as strong candidates as some of the other sources. The objects in this sample satisfy the color conditions in one plane, but not the other. As previously explained, this does not make them “weak” candidates; they are just not as strong as some of the other sources. Due to this, they will not be included in the final sample of this work.

7.3 CLASH survey

The second part of this thesis is to search for pop III galaxies using galaxy clusters as gravitational lenses. The data is collected from the CLASH website (http://archive.stsci.edu/prepds/clash/). As the survey is gathering data during the course of this thesis, only six of the 25 scheduled clusters have been made accessible for the public.

The results from the catalogs generated by CLASH are compared to catalogs created by Lucia Guatia (postdoc at Stockholm University). These catalogs are prepared in a different way compared to CLASH. By using the SExtractor with different input parameters she has generated catalogs with varying conditions of object detection.

In addition to this, one of the clusters that have not yet been released will also be processed. This is MACS0717.5+3745; it is of interest since it has the largest Einstein radius ($\theta_{\mathrm{E}} = 55'' \pm 3''$) of all the CLASH-clusters. The mass distribution of this cluster is relatively shallow which further enhance the area with high magnification. Zitrin et al. (2009) estimate that the area which has a larger magnification than $\mu = 10$ is 3.5 arcmin^2.

In the following subsections we will process each of the clusters and discuss the candidates obtained from them.

The additional catalogs has been generated by using different constraints and input parameters. As a result of this, 10 catalogs have been created for each cluster with different conditions. Below, we discuss the different cases.

- *Case A.* This catalog is optimized for detecting point sources. The flux of the source must be detected with a significance of at least 2 standard deviations.

- *Case B.* Since objects that are magnified by a gravitational lens may be distorted, e.g. arcs, we need a script to search for those. This case does exactly that. By allowing objects with a higher number of continuos pixels to be included in the sample, these objects are detected. As the lensed arcs may be faint, the detection threshold is lower than in case A.

- *Case C.* This catalog is similar to case B, but the arcs are allowed to be even longer.

- *Case D.* The largest and faintest objects are collected in this case. The number of continuos pixels are allowed to be 100 and the detection threshold is set to 0.3 standard deviations.

- *Case NEW.* This case tries to separate all possible sources, including objects that appear close to bright sources e.g. a cluster galaxy. To do this, SExtractor can "de-blend" the sources, i.e. separate them from each other. By using this input it is possible that it sometimes treats faint arcs as many different sources. It is therefore important to inspect all candidates.

These different cases are used for both the Y_{105}- and J_{125}-bands, resulting in 10 different catalogs for each galaxy cluster. As these cases are not exclusive some objects may appear in more than one catalog; it is therefore important to check possible candidates if they appear in more than one data set for each cluster.

7.3.1 Abell 383

This cluster is located at $z = 0.187$ at RA 02:48:03.36, Dec -03:31:44.7, and is one of the clusters selected using X-ray radiation. It was the first galaxy cluster observed by CLASH and the observations took place between November 2010 and March 2011. The sample generated by CLASH contains 2857 sources.

To find suitable candidates we want to constrain the data set. The first condition we apply is that we require the object to be detected in all relevant filters with at least 5σ significance. This includes all filters in the color-color diagrams except for the bluest filter. As z-band dropouts are expected to have a significantly reduced signal in this filter, we do not require a 5σ detection here. The color for objects with lower detection significance is only a lower limit.

As CLASH observes a cluster at different times with different filters, the field of view (FoV) might change between filters. As a result of this, some objects lie outside the FoV for one filter but not the others.

In Fig. 7.13, all the objects that satisfied our color criteria are plotted. Some of the sources was located to the left of the marked area in the $Y - J$ vs. $J - H$ plane, which can indicate a zero-metallicity galaxy with strong Lyman-α radiation. However, these objects could be excluded since their color signatures could be explained by either diffraction spikes or edge effects.

Further, we apply a non-detection constraint in the optical filters since we do not expect any flux in this wavelength area for Y- or z-band dropouts. Sources that are detected here could be spurious and are therefore rejected from the sample.

All sources that were not detected in any optical filter were then scrutinized to ensure that they were not located e.g. in diffraction spikes.

After constraining the sample, one source satisfied all our conditions. This is an object that is located at RA 02:48:02.16 and Dec -03:32:39.12. One of the output parameters in the CLASH data set is an estimation of the most likely photometric redshift. For this object that value is $z_{\rm phot} = 1.74$. This could be due to that the colors of this candidate does not meet the classical dropout criteria established by Bouwens et al. (2011). This candidate will be called A383-1 for the remainder of this thesis.

A second candidate to the left of the marked area did also appear. As this in an implication of a pop III candidate with strong Lyman-α radiation, this object is not rejected, and will be called A383-2.

Now, we want to compare the results from this sample to the alternative catalogs. In these data sets we are using the same constraints to get comparable samples. A383-1 does not appear in any of the other catalogs. However, other interesting sources appear. For instance is A383-2 not only detected, but it also satisfies the criteria for pop III candidates.

As many as 23 additional sources met our color criteria from this galaxy

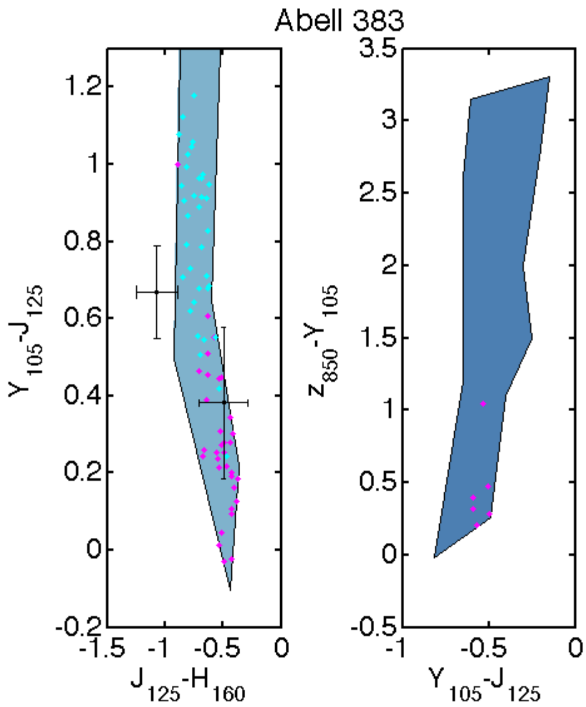

Figure 7.13: All objects that satisfied our color criteria in the sample obtained using the galaxy cluster Abell 383 as a gravitational lens. The blue data points represent objects which are located in diffraction spikes or very close to the edge of the FoV. These locations most likely affect the colors of the object, leading to an uncertain pop III candidate. The data points in magenta are sources detected with a 5σ detection significance in at least one of the optical bands.

cluster, and 22 of them were found in the $Y - J$ vs. $J - H$ color plane. Nine of the pop III candidates are presented in Fig. 7.14.

To avoid too many plots of all the different candidates the results are presented in Table 3. The fifth column show the most probable redshift of the object according to CLASH. If the source is not detected in their catalog, no estimate is given.

Of all the possible pop III candidates, only one has a likely redshift larger than 2, and that is A383-3 with $z_{\text{phot}} = 7.34$. Furthermore, one of the candidates, A383-2, appear in both the CLASH catalog as well as the additional data sets. The fact that this objects satisfies the conditions for both cases strengthens its position as a pop III candidate. The most probable redshift for A383-2 is $z_{\text{phot}} = 0.96$. The reason could be that even if the colors qualifies it as a classical dropout according to e.g. Bouwens et al. (2011), they also match the criteria for being an L or T dwarf star (Knapp et al., 2004), see Bouwens et al. (2011) for diagrams. However, even though this could be an interloper, it still satisfies our criteria in more than one data

Candidate	$z_{850} - Y_{105}$ (if applicable)	$Y_{105} - J_{125}$	$J_{125} - H_{160}$	z_{phot} (if applicable)
A383-1	> -0.23	0.38 ± 0.20	-0.50 ± 0.21	1.74
A383-2[a]	-	0.70 ± 0.05	-1.11 ± 0.09	0.96
A383-3	> -0.18	0.56 ± 0.08	-0.75 ± 0.11	7.34
A383-4	> -0.43	0.53 ± 0.18	-0.61 ± 0.23	1.73
A383-5	> 0.59	0.48 ± 0.07	-0.65 ± 0.09	0.90
A383-6	> -0.28	0.26 ± 0.17	-0.48 ± 0.23	-
A383-7	> 0.69	0.19 ± 0.07	-0.44 ± 0.09	0.90
A383-8	> -0.34	0.16 ± 0.20	-0.57 ± 0.33	-
A383-9	> 0.01	-0.04 ± 0.15	-0.48 ± 0.23	-
A383-10	> -0.17	0.24 ± 0.15	-0.86 ± 0.27	-
A383-11	> 0.09	0.32 ± 0.12	0.43 ± 0.16	1.57
A383-12	> -0.11	0.58 ± 0.12	-0.63 ± 0.15	1.76
A383-13	> -0.13	0.13 ± 0.15	-0.59 ± 0.24	1.09
A383-14	> -0.30	0.10 ± 0.17	-0.54 ± 0.25	-
A383-15[b]	> 0.82	-0.44 ± 0.05	0.31 ± 0.06	1.34
A383-16	> -0.57	0.35 ± 0.20	-0.50 ± 0.23	1.76
A383-17	> 0.63	0.27 ± 0.07	-0.43 ± 0.09	-
A383-18	> -0.32	0.24 ± 0.16	-0.46 ± 0.22	1.59
A383-19	> -0.25	0.20 ± 0.16	-0.48 ± 0.22	-
A383-20	> 0.63	0.27 ± 0.07	-0.43 ± 0.09	1.77
A383-21	> -0.38	0.55 ± 0.16	-0.57 ± 0.20	1.73
A383-22	> -0.12	0.52 ± 0.07	-0.56 ± 0.09	-
A383-23	> 0.49	-0.05 ± 0.10	-0.68 ± 0.18	0.48
A383-24	> -0.51	0.68 ± 0.17	-0.84 ± 0.24	-
A383-25	> -0.39	0.32 ± 0.17	-0.59 ± 0.25	1.66

Table 3: All the candidates in Abell 383 from both the CLASH sample and the alternative data sets.
[a] In the z_{850}-band, the source is outside the FoV. Hence, no estimate of the magnitude in that filter is possible.
[b]This candidate met the criteria in the $z - Y$ vs. $Y - J$ diagram.

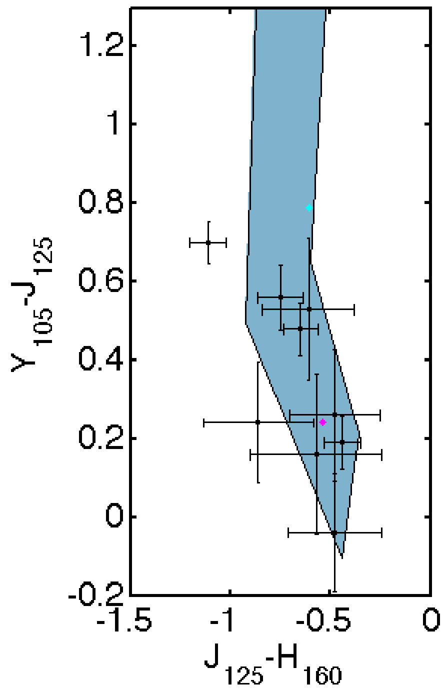

Figure 7.14: Nine of the pop III candidates obtained from the catalogs from the galaxy cluster Abell 383.

catalog with different constraints, which makes it an intriguing source.

A383-2 and A383-3 are therefore the strongest candidates in this cluster and follow-up spectroscopy of these objects could either confirm or reject them as reliable pop III galaxy candidates.

7.3.2 Abell 2261

This cluster is located at RA 17:22:27.25 and Dec +32:07:58.6 at a redshift of $z = 0.224$. It was observed from March to May 2011.

The CLASH sample contains 2127 objects and 13 of them met our criteria in either $Y - J$ vs $J - H$ or $z - Y$ vs. $Y - J$ criteria. However, 12 of them were excluded due to detection in at least one of the optical bands. The last possible candidate was found to be located in a spike from a nearby star and was therefore rejected.

In the alternative catalogs, however, 2 possible pop III galaxy candidates were uncovered. Fig. 7.15 shows their placements in the color diagrams. The candidate in Fig. 7.15a also meet the criteria in case C in Y_{105}, while the candidate in Fig. 7.15b satisfies the conditions for both case B and D in J_{125}. In this thesis these candidates will be referred to as A2261-1 and

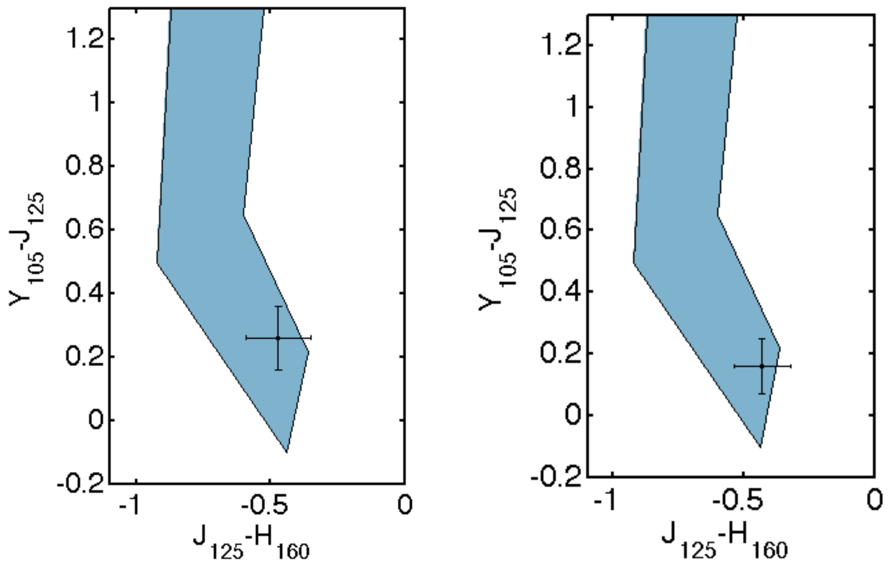

(a) **(b)**

Figure 7.15: (a) A2261-1 in the $Y-J$ vs. $J-H$ plane. This plot represent the colors in case B obtained from the Y_{105}-band. (b) A2261-2 from in case B in J_{125}.

A2261-2, respectively.

A2261-1 is not detected in the CLASH catalog, but A2261-2 is. However, by using the magnitudes given in that sample, the colors do not meet our criteria, even if the data point lies just outside the marked surface. The most probable redshift for this candidate is $z_{\rm phot} = 6.52$ according to CLASH. This makes this source an interesting candidate.

7.3.3 MACS 1149

MACS 1149 is a galaxy cluster that was selected due to its suitability as a gravitational lens. It is located at redshift $z = 0.544$ at RA 11:49:35.86 and Dec +22:23:55.0. It was observed between December 2010 and March 2011. The final sample contains 2355 objects.

However, even if this cluster has a high magnification, no object that satisfied our conditions were found in the CLASH catalog.

By examining the other data sets for this cluster no additional candidates were found; 17 sources matched our color criteria but all of them could be excluded due to detection in optical bands or diffraction spikes.

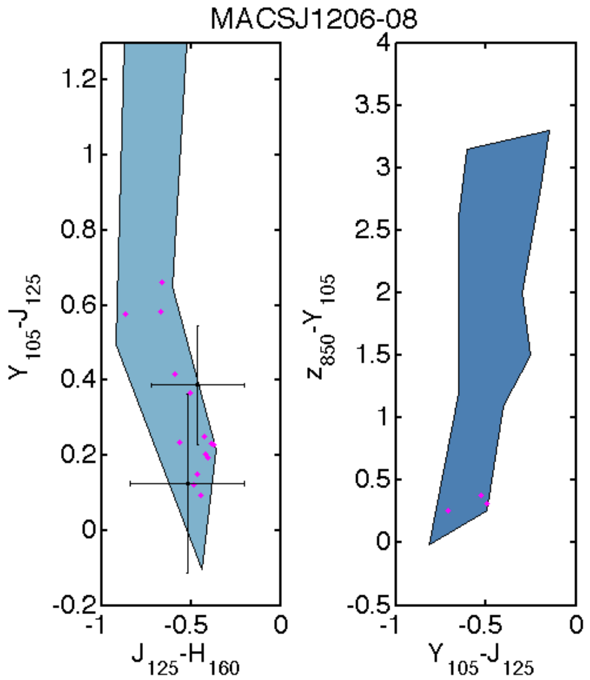

Figure 7.16: Objects that met our criteria in the MACS 1206 sample obtained from CLASH.

7.3.4 MACS 1206

MACS 1206 was selected using X-ray observations. It is situated at RA 12:06:12.28 and Dec -08:48:02.4 and has $z = 0.440$. The sample catalog generated by CLASH contains 2202 objects.

After applying our constraints on the objects, two sources that meet our criteria in the $Y - J$ vs. $J - H$ plane are left. These are presented in Fig. 7.16.

The candidate with $Y - J \approx 0.4$ will, for the remainder of this thesis, be referred to as M1206-1 and the other M1206-2. The most likely redshifts for these objects according to CLASH is $z = 1.59$ and $z = 6.30$, respectively.

By exploring the additional data sets, M1206-2 was detected in case NEW in the J_{125}-band. In this catalog the candidates also satisfied the color-criteria, further strengthening its status as a reliable pop III galaxy candidate.

A third candidate in this cluster was also uncovered in case B and D in J_{125}; it will be noted as M1206-3. This objects is also detected in the CLASH-catalog but end up outside the color criteria. However, the most likely redshift for this object is $z = 6.38$ according to CLASH estimates.

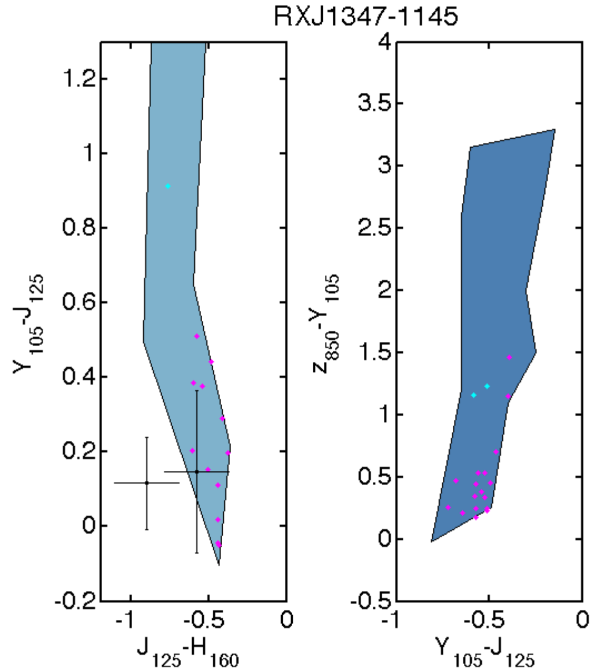

Figure 7.17: Objects that satisfied our color criteria from the RXJ 1347 data catalog generated by CLASH.

7.3.5 RXJ 1347

Located at RA 13:47:30.59 and Dec -11:45:10.1 with a redshift of $z = 0.451$, this is one of the X-ray selected galaxy clusters. The observations took place between April and July of 2011. The data set generated by CLASH contains 2102 objects.

The conditions that we applied to the data set constrained the catalog to two possible pop III galaxy candidates in the $Y - J$ vs. $J - H$ color plane. These are presented in Fig. 7.17. One of these candidates are located outside the marked surface in the color-color plane. However, as mentioned previously, this location could indicate a non-metallicity objects with a strong Lyman-α radiation. It is therefore kept as a viable candidate.

The source that met our criteria will be called RXJ-1 and the object to the left of the area will be referred to as RXJ-2. The most likely redshift for RXJ-1 is $z = 6.33$ while the corresponding value for RXJ-2 is $z = 6.62$.

The additional catalogs are also narrowed down to two objects, and it just happens to be both RXJ-1 and RXJ-2. RXJ-2 is detected in case B in the J_{125}-band and RXJ-1 is detected in both case A and NEW in the same filter. The fact that both CLASH and the additional catalogs give the same candidates further strengthen their status as pop III galaxy candidates. However, after a closer inspection of RXJ-1 it was revealed that it seems to

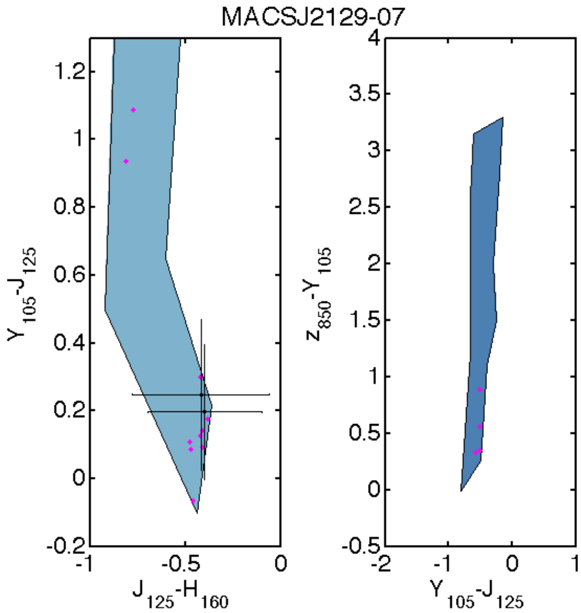

Figure 7.18: Objects that satisfied our color criteria from the MACS 2129 catalog generated by CLASH. The colors of the data points represent the same thing as in previous diagrams.

be one of two interacting galaxies which can explain the extreme colors. RXJ-1 was therefore excluded from the final sample.

7.3.6 MACS 2129

This galaxy cluster is located at a redshift of $z = 0.570$ at RA 21:29:26.06 and Dec -07:41:28.8. It is one of the clusters that have been selected due to its high magnification. The observations took place between May and July in 2011 and the final catalog created by CLASH contains 2146 sources.

After applying the same conditions as for the other data sets, we were left with two candidates in the $Y - J$ vs. $J - H$ plane. Their locations in this plot are displayed in Fig. 7.18.

The candidate with the largest value of $Y - J$ will be referred to as M2129-1 while the second candidate will be denoted M2129-2. The most likely redshift for M2129-1 is $z = 1.59$ while the corresponding value for M2129-2 is $z = 0.93$, according to CLASH. The reason for their low values could be that they are not classified as classical dropouts (e.g. Bouwens et al., 2011).

When studying the additional catalogs, three further candidates were discovered. In Fig. 7.19, two of them are presented. The candidate in the $Y - J$ vs. $J - H$ plane will be referred to as M2129-3 while the one in the $z - Y$ vs. $Y - J$ diagram will have the notation M2129-4. M2129-4 was also

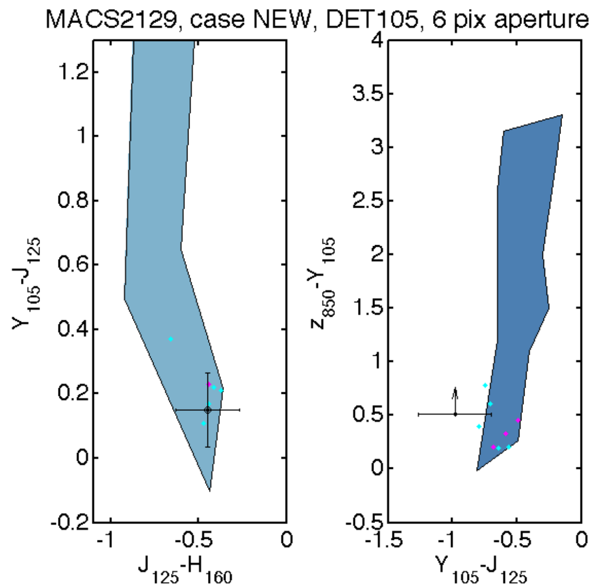

Figure 7.19: M2129-3 and M2129-4 in their respective color-color diagram.

detected in case B and C in the J_{125}-band.

M2129-3 is detected in CLASH but end up outside our color criteria. Additionally, they estimate the most likely redshift to be $z = 0.81$. It is the same case for the other candidate, M2129-4; it is detected in their survey but does not satisfy our conditions and the most likely redshift is $z = 0.65$.

A third source, M2129-5, met our color criteria in the additional catalogs. It is detected in the $Y - J$ vs. $J - H$ plane and is plotted in Fig. 7.20. This object does not occur in the CLASH data set.

7.3.7 MACS 0717

The final cluster is one of the high magnification clusters. It is located at RA 07:17:31.65 and Dec +37:45:18.5 with a redshift of $z = 0.548$. The observations of this galaxy cluster took place between August and September of 2011. However, the data from CLASH is not yet accessible for the public; it will be released in July 2012, at the earliest. Due to this, we only have the alternative data sets at hand.

Four possible candidates were uncovered in the catalogs, where three of them were found in the same set. These are presented in Fig. 7.21. From top to bottom, their notations are M0717-1, M0717-2 and M0717-3. M0717-3 appears in three other catalogs, while M0717-1 and M0717-2 only occur in this one.

Apart from the three sources detected in case NEW in the J_{125}-filter, a fourth object was found in another data set. M0717-4 in case NEW in the

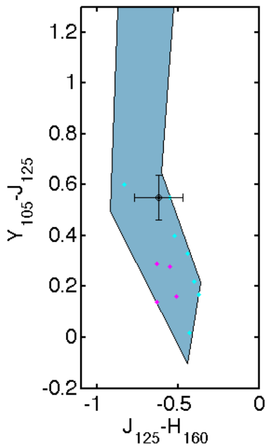

Figure 7.20: M2129-5 in a $Y-J$ vs. $J-H$ plot. Other sources in the catalog met our color criteria but could be ruled out due to e.g. diffraction spikes.

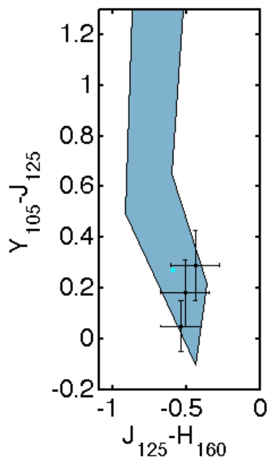

Figure 7.21: M0717-1, M0717-2 and M0717-3 in case NEW in J_{125}-band.

Y_{105}-filter is shown in Fig. 7.22.

8 Summary

As galaxies at high redshift are expected to show a break at the Lyman-α wavelength, 1216 Å, the fluxes in two neighboring filters can vary significantly if this break occurs in one of them. The colors obtained from using these filters may then be more extreme than for low-redshift objects. By using this feature in the spectrum it is possible to construct distinguishable conditions for galaxies at high redshift.

However, as we are searching for pop III galaxies in this survey, it is not sufficient to only find the characteristics of high-redshift galaxies. It is equally important to find distinct features of pop III galaxies.

To determine the colors of zero-metallicity high redshift galaxies, we use

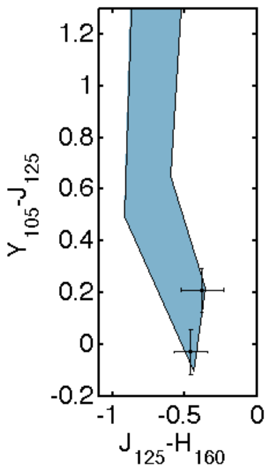

Figure 7.22: M0717-4 in case NEW in the Y_{105}-band. The candidate at the lower end of the marked area is M0717-3.

the program Yggdrasil, a spectral synthesis code which predicts e.g. the magnitudes for different types of galaxies. This code can not only handle different metallicities, but also age, extinction, Lyman-α radiation etc. By using this code with a variety of input parameters we have managed to find unique areas in color-color diagrams that exclusively harbor pop III galaxies at high redshift.

The results originate partly from published samples of high-redshift galaxies obtained from UDFs. The galaxies were identified by using the significative Lyman break and a number of them matched the color criteria derived from Yggdrasil. As two of them satisfied our criteria in more than one color-color plane these are considered stronger candidates. Additionally, two other sources were not only identified in more than paper, but also met our color criteria. Hence, these are also considered relatively strong candidates.

As galaxy clusters are very massive they provide us with an excellent tool for observing the high-redshift universe. Light that travels through the cluster is deflected by the massive object. As a results of this, the area behind the cluster is magnified and the fluxes of background objects are boosted, allowing objects that are intrinsically faint to be observed.

CLASH is currently observing 25 galaxy clusters in 16 different filters in search for e.g. high-redshift objects. At the start of this thesis, data from six of these clusters had been released to the public and these catalogs were processed to find viable candidates. To increase the possibility of finding pop III candidates, additional catalogs were generated by Lucia Guatia at Stockholm University, to possibly confirm reliable candidates and discover additional objects. These catalogs were created using different detection conditions to ensure a complete data set. Objects that are gravitationally lensed can have different appearances; they can be faint arcs of different sizes. The catalogs are therefore designed to favor different shapes and brightnesses

Candidate	RA (J2000)	Dec (J2000)	$z_{850} - Y_{105/098}$ (if applicable)	$Y_{105} - J_{125}$	$J_{125} - H_{160}$
HUDF_2836[b]	03:32:35.05	-27:47:25.8	$0.59^{+0.45}_{-0.34}$	$-0.48^{+0.50}_{-0.37}$	$-0.07^{+0.50}_{-0.37}$
ERS_9923[a,b]	03:32:29.69	-27:45:22.6	> 1.10	$-0.54^{+0.34}_{-0.28}$	$0.07^{+0.32}_{-0.26}$
HUDF_2324[b]	03:32:41.60	-27:47:04.5	$0.79^{+0.39}_{-0.31}$	$-0.16^{+0.27}_{-0.23}$	$-0.20^{+0.30}_{-0.26}$
ERS_9041[a,b]	03:32:23.37	-27:43:26.5	–	> 1.25	$-0.68^{+0.39}_{-0.29}$
A383-2[b,c]	02:48:02.54	-03:32:12.69	–	0.70 ± 0.05	-1.11 ± 0.09
A383-3[b]	02:48:02.14	-03:32:39.28	> -0.18	0.56 ± 0.08	-0.75 ± 0.11
A2261-2[c]	17:22:24.15	32:07:27.63	> -0.036	-0.054 ± 0.13	-0.21 ± 0.19
M1206-2[c]	12:06:17.09	-08:48:11.35	> -0.37	0.12 ± 0.24	-0.52 ± 0.32
M1206-3	12:06:10.01	-08:48:44.12	0.53 ± 0.34	0.05 ± 0.15	-0.08 ± 0.15
RXJ-2[c]	13:47:31.76	-11:44:31.86	> -0.29	0.12 ± 0.12	-0.90 ± 0.21
M0717-3	07:17:38.18	37:45:16.88	-0.11 ± 0.19	0.01 ± 0.09	-0.43 ± 0.11

Table 4: The strongest candidates from both the UDFs and the lensed fields.
[a]Candidates where the Y_{098}-filter has been used.
[b]Candidates which are considered classical dropouts (Bouwens et al., 2011; Wilkins et al., 2011).
[c]Sources which are considered pop III galaxy candidates in both the CLASH catalogs and the additional data sets.

of the detected objects.

After applying our constraints and color criteria, we discovered a number of candidate objects. These were then inspected to make sure that their signatures could not be explained by e.g. diffraction spikes or edge effects. We were then left with a sample of reliable pop III galaxy candidates and their details and properties are presented in Table 4, with their coordinates and colors. In Figs. 8.1 and 8.2 images of the candidates in all relevant filters are presented.

9 Discussion

Using color signatures is a relatively uncomplicated way of finding pop III galaxy candidates. However, it is important to account for all different conditions a galaxy of this type can harbor. Throughout this thesis we have assumed that all stars in the galaxy were formed at one time, i.e. an instantaneous burst, even if the best approximation would have been that the galaxy had experienced a continuos star formation rate. However, taking this into account would significantly increase the time spent on the construction of the color criteria.

From Fig. 7.3 we see that the resulting color criteria generated by Yggdrasil are not entirely within the borders of classical dropouts (Bouwens et al., 2011; Wilkins et al., 2011). Generally, the pop III galaxies with strong Lyman-α radiation have to be located at a higher redshift to satisfy the classical dropout conditions. As a result of this, only applying the conditions given in the papers might lead to excluding true pop III galaxy candidates.

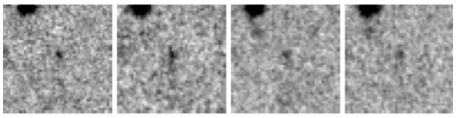

(a) HUDF_2836

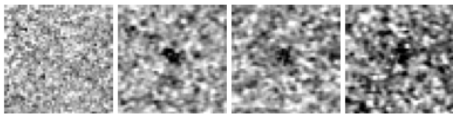

(b) ERS_9923

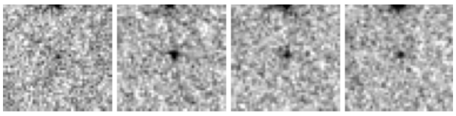

(c) HUDF_2324

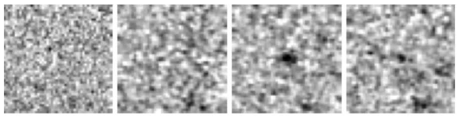

(d) ERS_9041

Figure 8.1: Thumbnails ($3'' \times 3''$) of the candidates obtained using UDFs. The filters are, from left to right, z_{850}, $Y_{105/098}$, J_{125} and H_{160}. Credit: McLure et al. (2011).

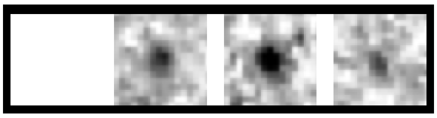

(a) A383-2

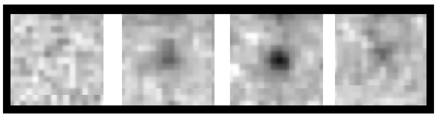

(b) A383-3

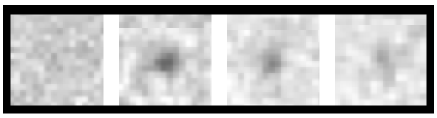

(c) A2261-2

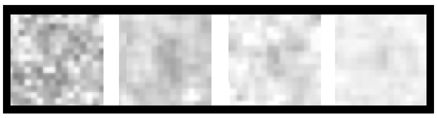

(d) M1206-2

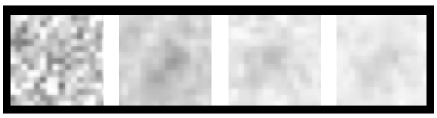

(e) M1206-3

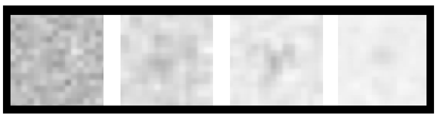

(f) RXJ-2

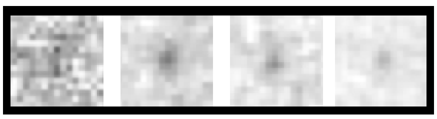

(g) M0717-3

Figure 8.2: Thumbnails ($1'' \times 1''$) of candidates obtained from the gravitationally lensed fields. The filter are, from left to right, z_{850}, Y_{105}, J_{125} and H_{160}.

Using the conditions generated by Yggdrasil, one could extend the sample of pop III galaxy candidates. Finding objects that satisfy both the classical dropout criteria as well as meeting the conditions generated in this thesis would therefore be strong pop III galaxy candidates. When constructing the color criteria for pop III galaxies we only used the evolutionary tracks for high-redshifts as they are expected to be located at $z > 6$. However, it is possible that lower redshift objects have similar colors and therefore enter the sample. For instance may L and T dwarfs meet the classical dropout criteria in the $Y_{105} - J_{125}$ vs. $J_{125} - H_{160}$ plane (Knapp et al., 2004; Bouwens et al., 2011) and it is important to be cautious with sources meeting these conditions.

Worth noticing is that in this thesis we have assumed that pop III galaxies consist solely of pop III stars. However, it is possible that these galaxies may harbor more chemically advanced stars, i.e. pop I/II stars (Stiavelli & Trenti, 2010), which can alter the observed overall spectrum. Additionally, the IMF of the stars in the early universe is currently uncertain; it may favor less massive stars than what is currently believed (e.g. Stacy et al., 2010). If this is the case, it will impact the observable signatures of pop III galaxies. In this thesis, however, we have used different types of IMFs to account for this possibility.

The conditions of our color criteria are related to the redshift and each pop III-region in the color-color diagrams range over different redshifts. However, these redshift spans overlap. Finding objects that satisfy both color conditions would therefore make strong candidates. Objects that only meet the criteria in one of the diagrams are not necessarily "bad" candidates; they are just not as strong as sources in both. The redshifts of the objects that meet the criteria in both planes can be estimated using three (instead of two) colors with the evolutionary tracks provided by Yggdrasil. If the values of these redshift estimates match, it is a suitable high-redshift pop III galaxy candidate.

Some of the objects that meet our color criteria are detected in both the catalog that CLASH generated as well as in one or more of the additional data sets. Of course, detection in more that one catalog improve the chances of it actually being a pop III galaxy and not an interloper. However, as the catalogs are using different constraints to construct a sample, an object which is detected in the CLASH catalog but not in any other does not have to be a questionable candidate. As described in Sect. 7.3 the additional catalogs are designed to detect different types of objects. A source that has been distorted to an arc by gravitational lensing is more likely to be detected in case B, C or D than case A.

As the data catalogs from CLASH are being released continuously, processing the data sets as they are released will probably result in more pop III galaxy candidates. As the current highest redshift detection of a galaxy (Lehnert et al., 2010) is being questioned, perhaps it is possible to find objects that break the highest redshift record.

Using color signatures as a way of discovering high-redshift pop III galaxy candidates is a relatively straightforward technique, but the discovered objects remain candidates. To confirm their high redshift, it is necessary to be able perform spectroscopy. As some of the candidates in this thesis are bright enough, it is our hopes that at least one will be confirmed as a high redshift object.

Acknowledgements

My first and greatest thanks goes of course to my thesis supervisor, **Erik Zackrisson**, who has helped with bot trivial and non-trivial problems. Not once has he been to busy to take the time for a simple master student, which I am extremely grateful for. I am also thankful for including me in the work of our paper (Zackrisson et al., 2012). I couldn't have asked for a better supervisor!

My second thanks goes to **Lucia Guaita** for preparing the additional catalogs for the CLASH clusters, as well as answering my questions about them.

My time in the master program would have been a lot less pleasant without my office mates and fellow students at the university. **Katia**, **Saghar**, **Anil**, **Atefeh** and **Alessandro**; we got to have another fondue evening!

I would also like to take the opportunity to thank for the nice treatment from all the people at the department of Astronomy at AlbaNova, and for all the nice "fikas" in the Wild West!

References

Bouwens R. J. et al., 2011, ApJ, 737, 90

Bradač M. et al., 2009, ApJ, 706, 1201

Bromm V., Yoshida N., 2011, Annual Review of Astronomy and Astrophysics, 49, 373

Calzetti D., 1997, in American Institute of Physics Conference Series, Vol. 408, American Institute of Physics Conference Series, W. H. Waller, ed., pp. 403–412

Ferland G. J., Korista K. T., Verner D. A., Ferguson J. W., Kingdon J. B., Verner E. M., 1998, PASP, 110, 761

Finkelstein S. L., Papovich C., Giavalisco M., Reddy N. A., Ferguson H. C., Koekemoer A. M., Dickinson M., 2010, ApJ, 719, 1250

Greif T. H., Bromm V., 2006, MNRAS, 373, 128

Greif T. H., Johnson J. L., Bromm V., 2008a, in American Institute of Physics Conference Series, Vol. 990, First Stars III, B. W. O'Shea & A. Heger, ed., pp. 405–417

Greif T. H., Johnson J. L., Bromm V., Klessen R. S., 2007, ApJ, 670, 1

Greif T. H. et al., 2008b, in IAU Symposium, Vol. 255, IAU Symposium, L. K. Hunt, S. Madden, & R. Schneider, ed., pp. 33–48

Heger A., Fryer C. L., Woosley S. E., Langer N., Hartmann D. H., 2003, ApJ, 591, 288

Johnson J. L., 2011, ArXiv e-prints 1105.5701

Johnson J. L., Greif T. H., Bromm V., 2008, MNRAS, 388, 26

Jones T., Stark D. P., Ellis R. S., 2011, ArXiv e-prints 1111.5102

Knapp G. R. et al., 2004, AJ, 127, 3553

Kroupa P., 2001, MNRAS, 322, 231

Lehnert M. D. et al., 2010, Nature, 467, 940

Leitherer C. et al., 1999, The Astrophysical Journal Supplement Series, 123, 3

Lorenzoni S., Bunker A. J., Wilkins S. M., Stanway E. R., Jarvis M. J., Caruana J., 2011, MNRAS, 414, 1455

Maizy A., Richard J., de Leo M. A., Pelló R., Kneib J. P., 2010, A&A, 509, A105

McLure R. J. et al., 2011, MNRAS, 418, 2074

Pei Y. C., 1992, ApJ, 395, 130

Postman M. et al., 2012, The Astrophysical Journal Supplement, 199, 25

Raiter A., Schaerer D., Fosbury R. A. E., 2010, A&A, 523, A64

Salpeter E. E., 1955, ApJ, 121, 161

Schaerer D., 2002, A&A, 382, 28

Shang C., Bryan G. L., Haiman Z., 2010, MNRAS, 402, 1249

Stacy A., Greif T. H., Bromm V., 2010, MNRAS, 403, 45

Steidel C. C., Giavalisco M., Pettini M., Dickinson M., Adelberger K. L., 1996, ApJL, 462, L17

Stiavelli M., Trenti M., 2010, ApJL, 716, L190

Tan J. C., McKee C. F., 2008, in American Institute of Physics Conference Series, Vol. 990, First Stars III, B. W. O'Shea & A. Heger, ed., pp. 47–62

Wambsganss J., 1998, Living Reviews in Relativity, 1, 12

Wilkins S. M., Bunker A. J., Lorenzoni S., Caruana J., 2011, MNRAS, 411, 23

Yoshida N., Abel T., Hernquist L., Sugiyama N., 2003, ApJ, 592, 645

Zackrisson E., Bergvall N., Olofsson K., Siebert A., 2001, A&A, 375, 814

Zackrisson E., Rydberg C.-E., Schaerer D., Östlin G., Tuli M., 2011, ApJ, 740, 13

Zackrisson E. et al., 2012, ArXiv e-prints 1204.0517

Zitrin A., Broadhurst T., Rephaeli Y., Sadeh S., 2009, ApJL, 707, L102